Monthly Notices of the ROYAL ASTRONOMICAL SOCIETY

MNRAS **516,** 5945–5963 (2022) https://doi.org/10.1093/mnras/stac2187
Advance Access publication 2022 August 6

The 'Giraffe': discovery of a stripped red giant in an interacting binary with an ∼2 $M_\odot$ lower giant

T. Jayasinghe [1,2]★ Todd A. Thompson [1,2] C. S. Kochanek,[1,2] K. Z. Stanek,[1,2] D. M. Rowan [1,2] D. V. Martin,[1,2]† Kareem El-Badry [3,4,5] P. J. Vallely [1,2] J. T. Hinkle [6] D. Huber,[6] H. Isaacson,[7,8] J. Tayar,[6,9] K. Auchettl,[10,11,12] I. Ilyin,[13] A. W. Howard[14] and C. Badenes[15]

[1]*Department of Astronomy, The Ohio State University, 140 West 18th Avenue, Columbus, OH 43210, USA*
[2]*Center for Cosmology and Astroparticle Physics, The Ohio State University, 191 W. Woodruff Avenue, Columbus, OH 43210, USA*
[3]*Center for Astrophysics | Harvard & Smithsonian, 60 Garden Street, Cambridge, MA 02138, USA*
[4]*Harvard Society of Fellows, 78 Mount Auburn Street, Cambridge, MA 02138, USA*
[5]*Max-Planck Institute for Astronomy, Königstuhl 17, D-69117 Heidelberg, Germany*
[6]*Institute for Astronomy, University of Hawai'i, 2680 Woodlawn Drive, Honolulu, HI 96822, USA*
[7]*Department of Astronomy, University of California Berkeley, Berkeley CA 94720, USA*
[8]*Centre for Astrophysics, University of Southern Queensland, Toowoomba, QLD 4305, Australia*
[9]*Department of Astronomy, University of Florida, Bryant Space Science Center, Stadium Road, Gainesville, FL 32611, USA*
[10]*OzGrav, School of Physics, The University of Melbourne, Parkville, Victoria 3010, Australia*
[11]*ARC Centre of Excellence for All Sky Astrophysics in 3 Dimensions (ASTRO 3D)*
[12]*Department of Astronomy and Astrophysics, University of California, Santa Cruz, CA 95064, USA*
[13]*Leibniz Institute for Astrophysics Potsdam (AIP), An der Sternwarte 16, D-14482 Potsdam, Germany*
[14]*Department of Astronomy, California Institute of Technology, Pasadena, CA 91125, USA*
[15]*Department of Physics and Astronomy and Pittsburgh Particle Physics, Astrophysics and Cosmology Center (PITT PACC), University of Pittsburgh, 3941 O'Hara Street, Pittsburgh, PA 15260, USA*

Accepted 2022 July 28. Received 2022 July 27; in original form 2022 January 26

ABSTRACT

We report the discovery of a stripped giant + lower giant Algol-type binary, 2M04123153+6738486 (2M0412), identified during a search for non-interacting compact object – star binaries. 2M0412 is an evolved ($T_{\rm eff,\,giant} \simeq 4000$ K), luminous ($L_{\rm giant} \simeq 150\,L_\odot$) red giant in a circular $P = 81.2$ d binary. 2M0412 is a known variable star previously classified as a semiregular variable. The cross-correlation functions of follow-up Keck/HIRES and LBT/Potsdam Echelle Polarimetric and Spectroscopic Instrument (PEPSI) spectra show an radial velocity variable second component with implied mass ratio $q = M_{\rm giant}/M_{\rm comp} \simeq 0.20 \pm 0.01$. The All-Sky Automated Survey for SuperNovae (ASAS-SN), Asteroid Terrestrial-impact Last Alert System (ATLAS), *Transiting Exoplanet Survey Telescope* (*TESS*), and Zwicky Transient Facility (ZTF) light curves show that the giant is a Roche lobe filling ellipsoidal variable with an inclination of $49.4 \pm 0.3°$, and a giant mass of $M_{\rm giant} = 0.38 \pm 0.01\,M_\odot$ for a distance of $\simeq$ 3.7 kpc. The mass of the giant indicates that its envelope has been partially stripped. The giant companion on the lower red giant branch has a mass of $M_{\rm comp} = 1.91 \pm 0.03\,M_\odot$ with $T_{\rm eff,\,comp} \simeq 5000$ K, $L_{\rm comp} \simeq 60\,L_\odot$, and $R_{\rm comp} \simeq 11\,R_\odot$. The lower giant contributes ∼35 per cent of the flux in the V band. We also identify an orbital phase dependent, broad Hα emission line which could indicate ongoing accretion from the stripped red giant on to the companion.

Key words: *(stars:)* binaries: spectroscopic – stars: individual: 2MASS J04123153+6738486.

1 INTRODUCTION

Rapid advances in time-domain astronomy and precision *Gaia* astrometry (Lindegren et al. 2021a) provide promising pathways for future discoveries of non-interacting compact objects. For example, Chawla et al. (2021) estimated that ∼30–300 non-interacting black holes (BHs) are detectable in binaries around luminous companions using astrometry from *Gaia*. Similarly, studies using binary population synthesis models have estimated that there are $\sim 10^2$–10^3 detached non-interacting BHs in the Milky Way (Shao & Li 2019; Langer et al. 2020; Janssens et al. 2022). In addition to astrometry, targeted searches combining high-cadence photometry and sparsely sampled radial velocities from wide-field time-domain surveys are a promising method to discover more systems (e.g. Trimble & Thorne 1969; Thompson et al. 2019; Zheng et al. 2019; Rowan et al. 2021).

Only a handful of convincing non-interacting compact objects have been discovered thus far. Three non-interacting BH candidates have been discovered in globular clusters: one by Giesers et al. (2018) in NGC 3201 (minimum BH mass $M_{\rm BH} = 4.36 \pm 0.41\,M_\odot$), and two by Giesers et al. (2019) in NGC 3201 [$M_{\rm BH} \sin(i) = 7.68 \pm 0.50\,M_\odot$

★ E-mail: jayasinghearachchilage.1@osu.edu
† NASA Sagan Fellow.

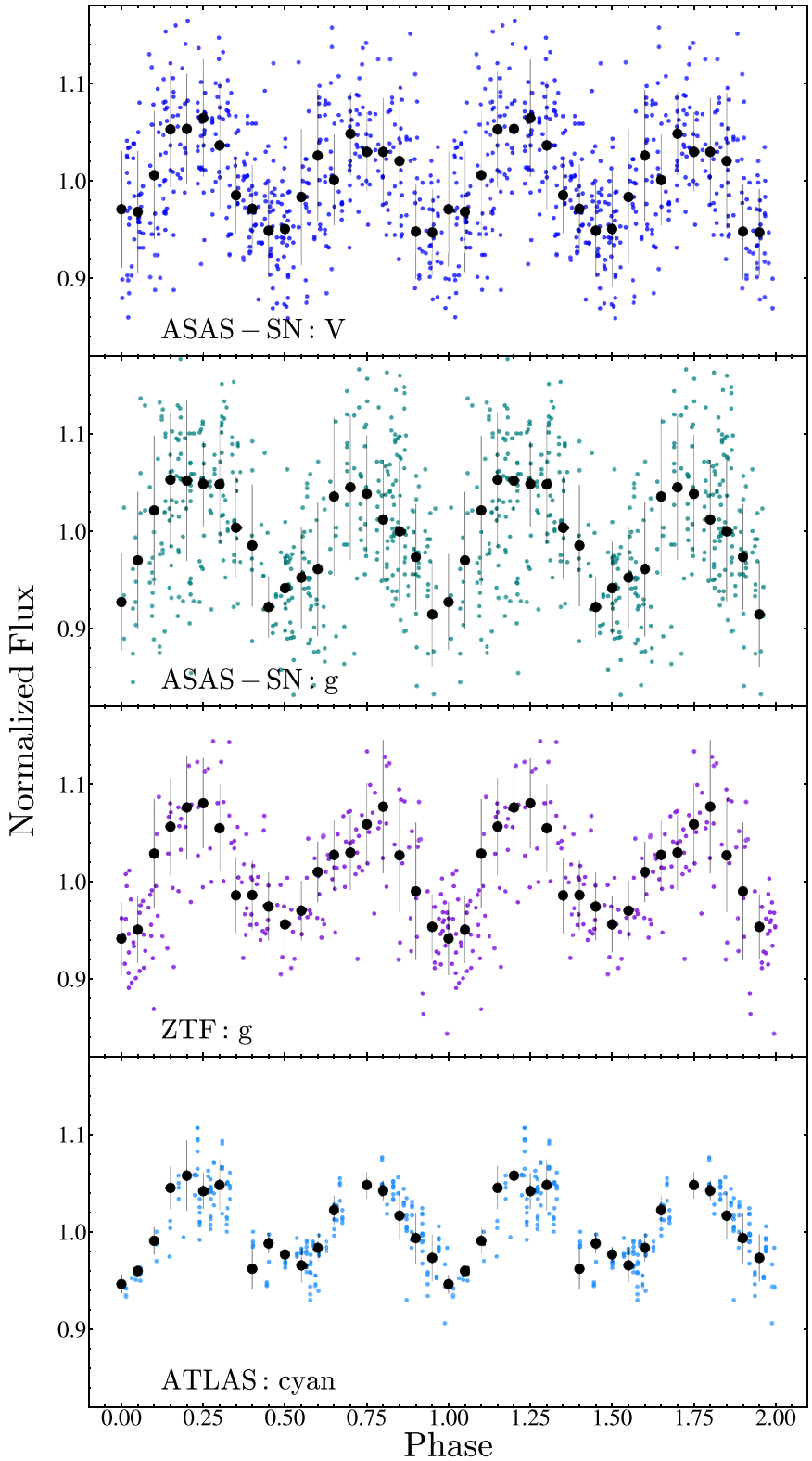

Figure 1. The normalized ASAS-SN *V*-, ASAS-SN *g*-, ZTF *g*-, and ATLAS *c*-band light curves for 2M0412 as a function of orbital phase (defined with the epoch of maximum RV at $\phi = 0.75$). The binned light curve for each data set is shown in black. The error bars for the binned light curve show the standard deviation.

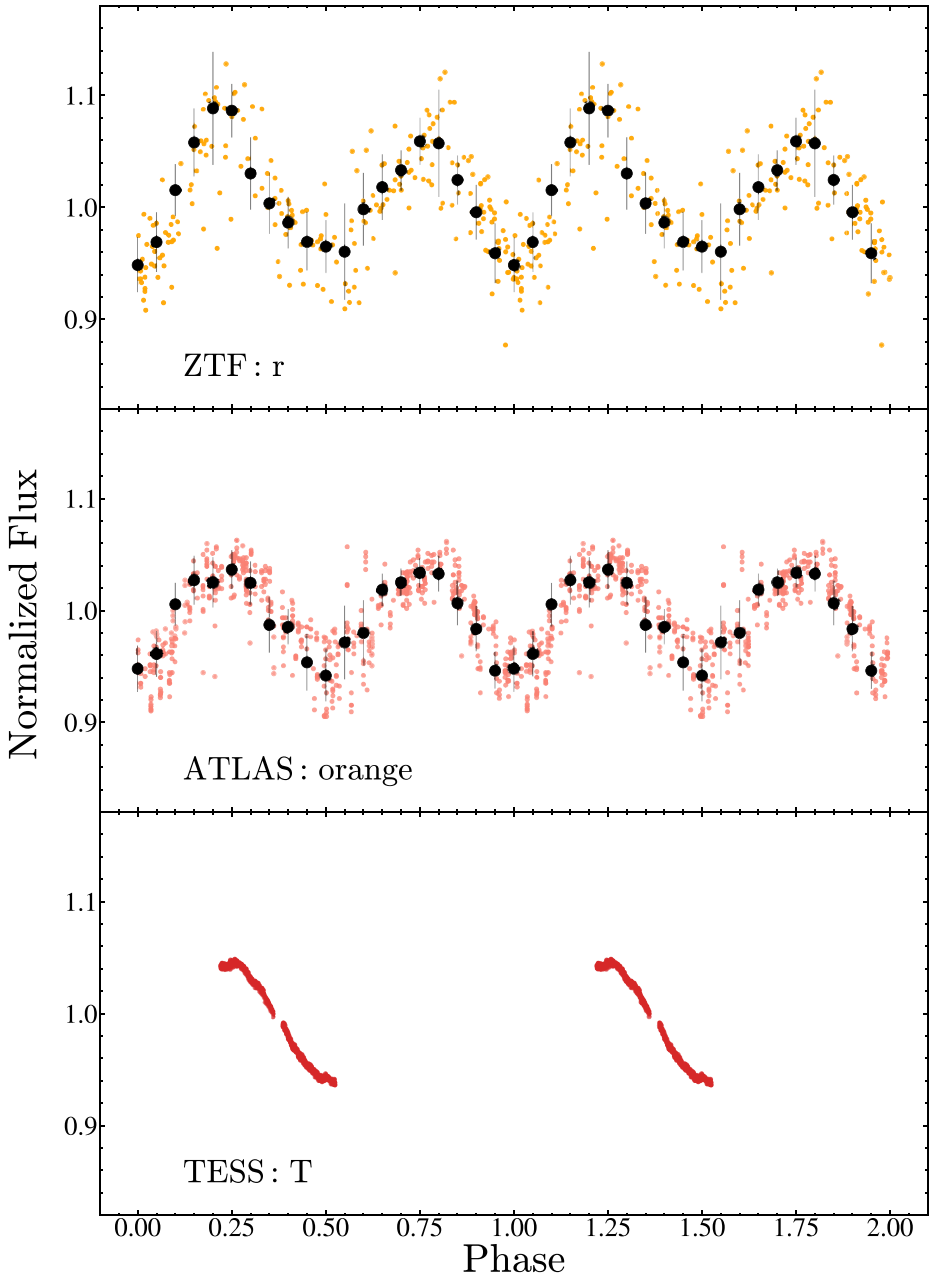

Figure 2. The normalized ZTF *r*-, ATLAS *o*-, and *TESS T*-band light curves for 2M0412. The format is the same as Fig. 1.

Table 1. *GALEX* and *Swift UV* observations.

JD	Date	Phase	Filter	AB mag limit	σ
2459453.807	2021-08-27	0.076	*Swift UVM2*	>22.78	3σ
2459488.654	2021-10-01	0.506	*Swift UVM2*	>22.67	3σ
2455572.568	2011-01-11	0.259	*GALEX NUV* (MIS)	>22.7	5σ
2453017.625	2004-01-13	0.782	*GALEX FUV* (AIS)	>19.9	5σ

and $M_{\rm BH}\sin(i) = 4.4 \pm 2.8\,{\rm M}_\odot$]. These systems all contain luminous main sequence companions. The globular cluster systems, if they indeed contain BHs, likely have formation mechanisms that are very different from those of field BH binaries because the high stellar densities allow formation mechanisms which do not operate for field stars. A single convincing non-interacting BH candidate has been found in the field. Thompson et al. (2019) discovered a low-mass ($M_{\rm BH} \simeq 3.3^{+2.8}_{-0.7}$ M$_\odot$) non-interacting BH candidate in

Table 2. Radial velocities from APOGEE DR16, HIRES, and PEPSI.

BJD (TDB)	Date	Phase	RV ($km\,s^{-1}$)	σ_{RV} ($km\,s^{-1}$)	Instrument
2457279.99438	2015-09-14	0.295	−86.888	0.031	APOGEE DR16
2457292.96813	2015-09-27	0.455	−59.246	0.016	APOGEE DR16
2457320.92338	2015-10-25	0.799	−7.964	0.023	APOGEE DR16
2457323.87005	2015-10-28	0.835	−11.194	0.017	APOGEE DR16
2459441.12722	2021-08-14	0.920	−26.94	0.10	HIRES
2459442.11471	2021-08-15	0.932	−30.43	0.10	HIRES
2459457.11748	2021-08-30	0.117	−74.32	0.10	HIRES
2459467.98696	2021-09-10	0.251	−87.423	0.060	PEPSI
2459472.12548	2021-09-14	0.302	−86.11	0.10	HIRES
2459485.12694	2021-09-27	0.462	−57.29	0.10	HIRES
2459489.96760	2021-10-02	0.522	−41.928	0.034	PEPSI
2459502.97527	2021-10-15	0.682	−9.84	0.10	HIRES
2459511.98487	2021-10-24	0.793	−7.61	0.10	HIRES
2459537.92734	2021-11-19	0.113	−73.81	0.10	HIRES

Table 3. Orbital elements for 2M0412.

Parameter	Joint RV data + `TheJoker`	Joint RV data + `TheJoker`	HIRES + `TheJoker`	Joint RV data + `yorbit`
P_{orb}(d)	81.439 ± 0.001	81.120 ± 0.001	81.136 ± 0.103	81.1643 ± 0.0029
K ($km\,s^{-1}$)	41.041 ± 0.138	40.976 ± 0.144	41.016 ± 0.138	41.038 ± 0.138
e	–	0.004 ± 0.003	–	–
ω (°)	0 (fixed)	341 ± 71	0 (fixed)	0 (fixed)
v_γ ($km\,s^{-1}$)	-47.137 ± 0.108	-47.096 ± 0.173	-47.217 ± 0.098	-47.031 ± 0.082
$a_{giant}\sin i$ ($R_\odot$)	65.846 ± 0.214	65.996 ± 0.359	65.840 ± 0.285	65.840 ± 0.285
$f(M)$ ($M_\odot$)	0.583 ± 0.006	0.578 ± 0.006	0.580 ± 0.006	0.581 ± 0.002

the field on a circular orbit at $P_{orb} \sim 83$ d around a spotted giant star.

However, the search for non-interacting compact objects is challenging, and numerous false positives have been identified. The binary LB-1 was initially thought to host an massive stellar BH ($M_{BH} \simeq 68^{+11}_{-3}$ $M_\odot$; Liu et al. 2019), but was later found to have a much less massive companion that was not necessarily a compact object (see e.g. Abdul-Masih et al. 2020; El-Badry & Quataert 2020; Irrgang et al. 2020; Shenar et al. 2020). The naked-eye system HR 6819 was claimed to be a triple system with a detached BH with $M_{BH} = 6.3 \pm 0.7$ $M_\odot$ (Rivinius et al. 2020), but was later found to be a binary system with a rapidly rotating Be star and a slowly rotating B star (Bodensteiner et al. 2020; El-Badry & Quataert 2021). Recently, NGC 1850 BH1 was claimed to be a binary displaying ellipsoidal variability in the Large Magellanic Cloud with $M_{BH} = 11.1^{+2.1}_{-2.4}$ $M_\odot$ (Saracino et al. 2022), but was later argued to be a stripped B star binary (El-Badry & Burdge 2022). Another example of a BH imposter was the system NGC 2004 #115, claimed to be a triple system consisting of a Be star on a tertiary orbit and an inner binary of a B star and a $\simeq$25 $M_\odot$ BH (Lennon et al. 2021). El-Badry, Burdge & Mróz (2022a) later argued that the orbital inclination was underestimated by assuming tidal synchronization, and that the companion to the B star was more likely an approximately 2–3 $M_\odot$ main-sequence star. Jayasinghe et al. (2021b) identified the nearby, nearly edge-on $P_{orb} = 59.9$ d circular binary V723 Mon as a candidate for a compact object – star binary. El-Badry et al. (2022b) later showed that V723 Mon is better explained by a stripped red giant in a binary around a massive ($\sim$2.8$M_\odot$), rapidly rotating subgiant. A common theme to these cases is an overestimate of the mass of the observed star based on its luminosity and the assumption of single star evolution for a binary where mass transfer has greatly reduced the mass of the more luminous star.

It is clear that binaries with ongoing or past mass transfer are an important false positive to understand in the search for non-interacting compact objects. In most of the cases discussed above, the more luminous companion is less massive than expected from single star evolution. Such binaries where the more evolved star is also the least massive component are categorized as Algol type binaries (Peters 2001) and are thought to emerge from Case B Roche lobe overflow (RLOF; Eggleton 1983). The final evolutionary end product of Algol binaries depends on the mass-transfer history. Algol binaries with RLOF are a formation channel for blue stragglers, barium stars, low mass helium white dwarfs, and carbon-enhanced metal poor stars (Collier & Jenkins 1984; Arentsen et al. 2019; Jorissen et al. 2019; El-Badry et al. 2021; Miller et al. 2021).

2M04123153+6738486 (hereafter 2M0412) is a luminous red-giant in the Camelopardalis constellation with J2000 coordinates (α, δ) = (63.13141144391°, 67.64683129470°). It was first classified as an 'NSINE' variable star (ATO J063.1314+67.6468) in the Asteroid Terrestrial-impact Last Alert System (ATLAS, Heinze et al. 2018; Tonry et al. 2018) catalogue of variable stars with a period of $\sim$80.36 d. It was classified as a semi-regular variable (ASASSN-V J041231.49+673848.6, ZTF J041231.52+673848.6) by the All-Sky Automated Survey for SuperNovae (ASAS-SN, Shappee et al. 2014; Jayasinghe et al. 2018, 2021a), and the Zwicky Transient Facility (ZTF, Bellm et al. 2019; Chen et al. 2020) with periods of $\sim$40.65 and $\sim$41.20 d, respectively. 2M0412 has four radial velocity measurements in the Apache Point Observatory Galactic Evolution Experiment DR16 (APOGEE, Gunn et al. 2006; Blanton et al. 2017; Wilson et al. 2019) with a maximum velocity difference

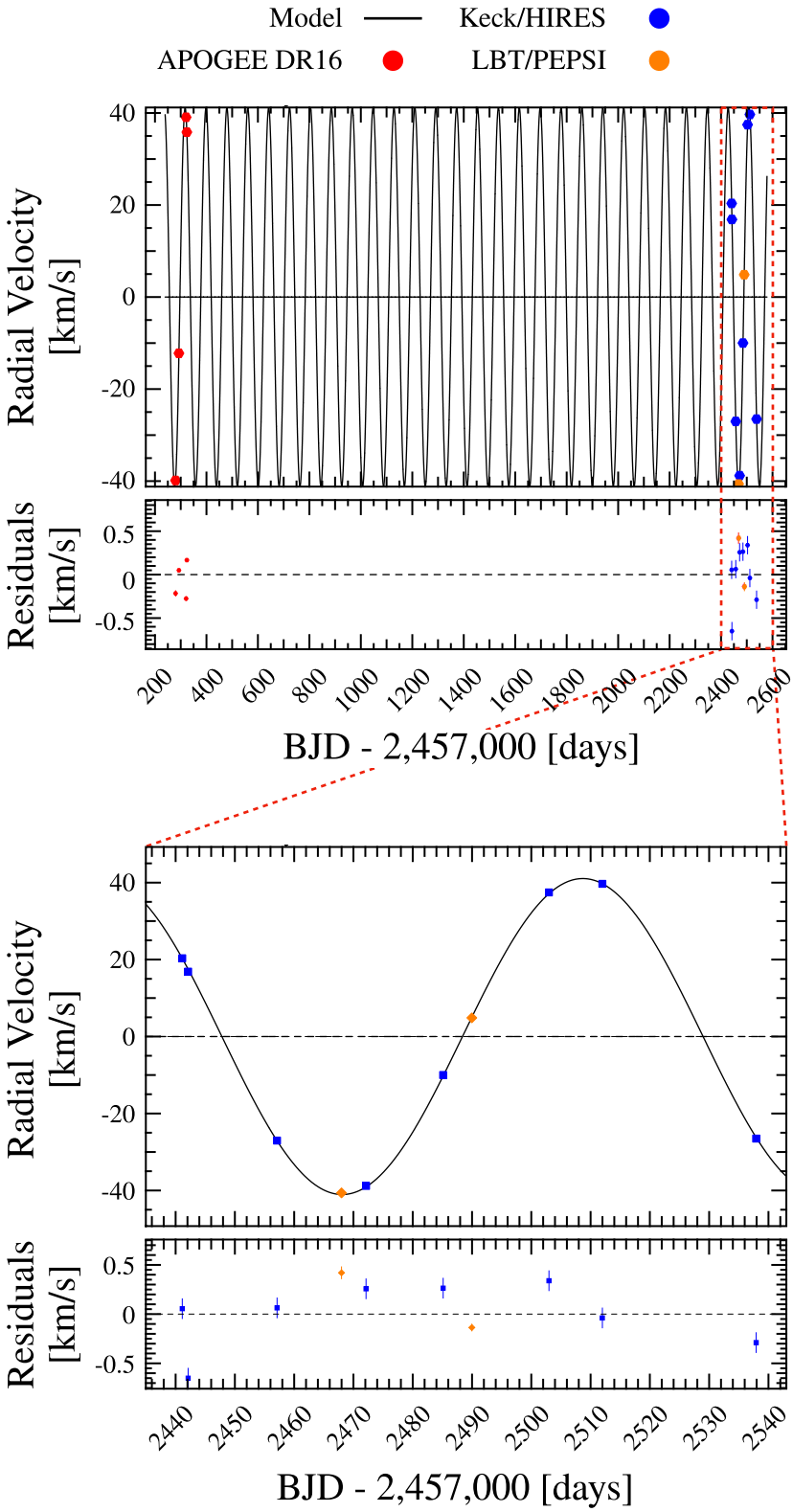

Figure 3. YORBIT radial velocity fit to the APOGEE, HIRES, and PEPSI data for the stripped red giant primary. The top figure shows the entire observational timespan. The bottom figure is zoomed into our follow-up measurements with HIRES and PEPSI, covering slightly more than one orbital period.

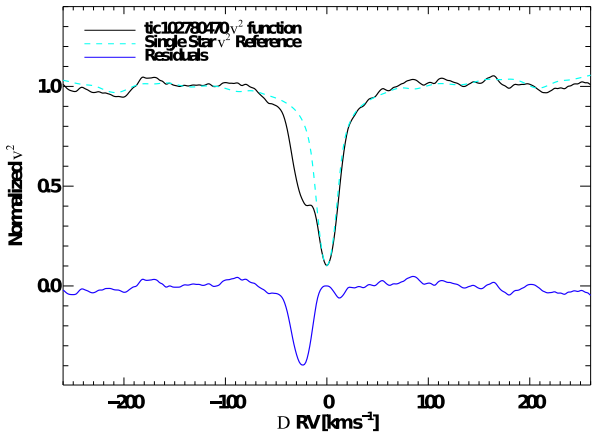

Figure 4. χ^2 as a function of the Doppler shift for the HIRES epoch at phase 0.92. The black line shows the observed rematch χ^2 function (Kolbl et al. 2015) for 2M0412. The light blue dashed line shows the expected χ^2 function for a single star. The dark blue line shows the residual χ^2 function after subtracting the single star reference.

of $\Delta RV_{\rm max} \sim 76$ km s^{-1} and a maximum observed acceleration between epochs of $\sim$1.7 km s^{-1} d^{-1} (Thompson et al. 2019). This led us to re-examine the light curves to realize that 2M0412 was in fact an ellipsoidal variable with an $\sim$81 d period. The radial velocity data and the orbital period from the light curves implied a mass function of $f(M) \simeq 0.5$ M$_\odot$, which led us to investigate the system in detail.

Here, we discuss our discovery of a $\sim$1.9 M$_\odot$ lower giant companion to the red giant in 2M0412. We initially considered this system as a viable candidate for a compact object – star binary. However, during the reviewing process of our manuscript, using the HIRES spectra collected in this work and archival APOGEE DR17 spectra, El-Badry et al. (2022b) showed that 2M0412 is better explained as an interacting Algol-type binary. We independently show that 2M0412 is an interacting binary composed of a stripped red giant and a more massive lower giant companion. In addition, we also provide evidence of ongoing binary interaction in this system. We describe the archival data and new observations used in our analysis in Section 2. In Section 3, we analyse the photometric and spectroscopic observations to derive the parameters of the binary system and the red giant. In Section 4, we compare the observations to binary population synthesis models. In Section 5, we discuss the nature of the companion. We present a summary of our results in Section 6.

2 OBSERVATIONS

Here we present observations, both archival and newly acquired, that are used in our analysis of 2M0412.

2.1 Distance, kinematics and extinction

In *Gaia* EDR3 (Gaia Collaboration 2021), 2M0412 is `source_id` = 4904508754036203 52. Its raw EDR3 parallax of $\varpi_{\rm EDR3} = 0.2310 \pm 0.0130$ mas implies a distance of $d = 1/\varpi = 4329 \pm 245$ pc. We correct the reported EDR3 parallax using the zero-point correction ($\simeq$39.89 μas) described in Lindegren et al. (2021a) which is dependent on the colour, magnitude, and sky position.[1]

[1]We calculate the parallax zero-point using the python script provided in https://gitlab.com/icc-ub/public/gaiadr3_zeropoint.

With this correction, we obtain $\varpi_{\rm EDR3,L21} = 0.2709 \pm 0.0130$ mas ($d = 1/\varpi = 3691 \pm 178$ pc). The global zero-point parallax offset in EDR3 is −17 μas (Lindegren et al. 2021a), and if we instead use this correction, we obtain $d = 1/\varpi = 4032 \pm 212$ pc. The zero-point correction from Lindegren et al. (2021a) differs from the global zero-point correction by approximately –23 μas. The probabilistic photogeometric distance estimate from Bailer-Jones et al. (2021) is $d = 3743^{+133}_{-161}$ pc. The spectrophotometric parallax estimate from Hogg, Eilers & Rix (2019) is $\varpi_{\rm spec} = 0.2284 \pm 0.0106$ mas ($d = 1/\varpi = 4378 \pm 204$ pc). The astrometric solution does not show significant excess noise and its renormalized unit weight error of 1.046 is not indicative of problems in the parallax or strong resolved binary motion. We adopt a distance of $d = 3.7$ kpc as our default.

At this distance, 2M0412 is $\sim$830 pc above the midplane. Its proper motion in EDR3 is $\mu_\alpha = -0.346 \pm 0.008$ mas yr^{-1}, and $\mu_\delta = 0.686 \pm 0.011$ mas yr^{-1}. Combining this with the systemic radial velocity from Section 3.1, the definition of the local standard of rest (LSR) from Schönrich, Binney & Dehnen (2010), and using `BANYAN` (Gagné et al. 2018) for the calculations, the three-dimensional space motion of 2M0412 relative to the LSR is $(U, V, W)_{\rm LSR} = (45.2, -19.5, -5.1)$ km s^{-1}. We calculated the thin disc, thick disc, and halo membership probabilities based on these velocities following Ramírez, Allende Prieto & Lambert (2013) to obtain $P(\text{thin}) \simeq 98.5$ per cent, $P(\text{thick}) \simeq 1.5$ per cent, and $P(\text{halo}) \simeq 0$ per cent, respectively. This suggests that this system is a kinematically normal object in the thin disc.

2.2 Light curves

We analysed well-sampled light curves from ASAS-SN, ATLAS, and ZTF, along with a densely sampled but phase-incomplete light curve from the *Transiting Exoplanet Survey Telescope (TESS)*.

The ASAS-SN (Shappee et al. 2014; Kochanek et al. 2017) survey obtained *V*- and *g*-band light curves of 2M0412 spanning from 2014 December to 2021 November ($\sim$31 orbits). 2M0412 clearly varies in the ASAS-SN light curves, with two equal maxima and two minima when phased with the orbital period. We determined the photometric period using `Period04` (Lenz & Breger 2005). The dominant ASAS-SN periods of $P_{\rm ASAS\text{-}SN,\,V} = 40.5930 \pm 0.0572$ d and $P_{\rm ASAS\text{-}SN,\,g} = 40.6090 \pm 0.08442$ d correspond to $P_{\rm orb}/2$ for ellipsoidal variability. We find an orbital period of

$$P_{\rm orb,\,ASAS-SN\,V} = 81.1861 \pm 0.1144 \text{ d}. \quad (1)$$

We retrieved *g*- and *r*-band photometry from the ZTF DR7 catalogue (Masci et al. 2019) spanning 2018 April to 2021 April ($\sim$13 orbits). The dominant periods in the ZTF data, $P_{\rm ZTF,\,g} = 40.7195 \pm 0.0770$ d, $P_{\rm ZTF,\,r} = 40.5224 \pm 0.0753$ d, again correspond to $P_{\rm orb}/2$. We also retrieved photometry from the ATLAS survey (Tonry et al. 2018) in the ATLAS '*c*' (cyan) and '*o*' (orange) filters. The ATLAS observations span from 2017 August to 2021 March ($\sim$16 orbits). We obtain photometric periods of $P_{\rm ATLAS,\,c} = 40.5497 \pm 0.0633$ d, $P_{\rm ATLAS,\,o} = 40.5447 \pm 0.0627$ d. The differences between the ASAS-SN, ZTF, and ATLAS photometric period estimates are not statistically significant.

2M0412 (`TIC 102780470`) was observed by *TESS* (Ricker et al. 2015) in Sector 19, and the 27 d of observations span [0.22,0.52] in orbital phase where the phase of the RV maximum is 0.75. We analysed the *TESS* data using the adaptation of the ASAS-SN image subtraction pipeline for analysing *TESS* full-frame images described in Vallely et al. (2021). The light curve does not include epochs where the observations were compromised by the spacecraft's momentum dump manoeuvers.

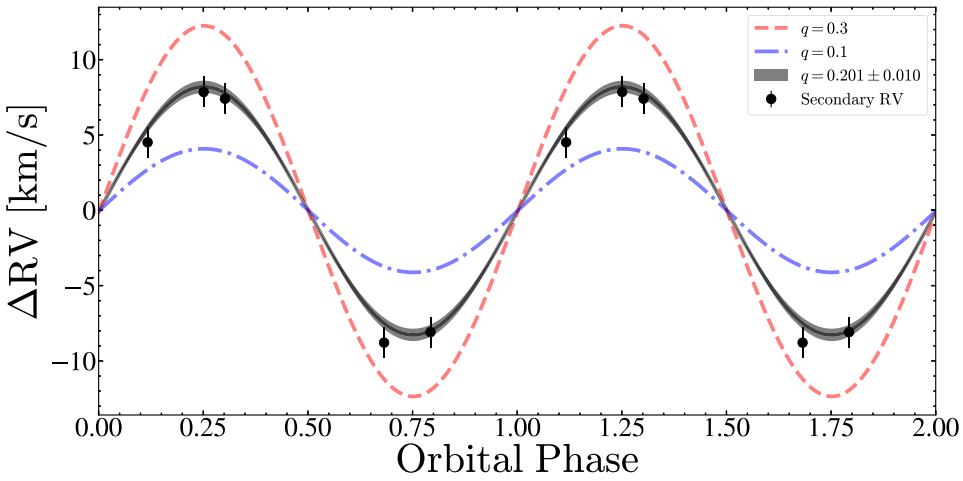

Figure 5. Orbital velocity as a function of phase for the second component in the HIRES and PEPSI spectra. The black shaded region illustrates the expected counter-motion of a component with a mass ratio $q = 0.201 \pm 0.010$. Theoretical RV curves for mass ratios of $q = 0.3$ and $q = 0.1$ are shown as red dashed and blue dot–dashed lines, respectively.

Table 4. Multiband photometry measurements used in the construction of the SED for 2M0412. Luminosities for each band are calculated assuming a nominal distance of $d \simeq 3.7$ kpc. The fluxes and luminosities have not been corrected for extinction.

Filter	Magnitude	σ	F_λ (ergs s^{-1} cm^{-2} Å^{-1})	λL_λ (L$_\odot$)	Reference
GALEX FUV	>19.9	5σ	$<7.1 \times 10^{-13}$	<0.296	AIS; Bianchi et al. (2014)
GALEX NUV	>22.7	5σ	$<2.5 \times 10^{-13}$	<0.015	MIS; Bianchi et al. (2014)
Swift UVM2	>22.8	3σ	$<1.0 \times 10^{-14}$	<0.004	This work
Johnson *B*	16.34	0.05	1.1×10^{-12}	4.0	Henden et al. (2018)
Johnson *V*	14.39	0.04	1.5×10^{-12}	16.8	Henden et al. (2018)
Pan-STARRS *g*	15.15	0.01	3.5×10^{-15}	9.7	Chambers et al. (2016)
Pan-STARRS *r*	13.55	0.01	9.5×10^{-15}	33.4	Chambers et al. (2016)
Pan-STARRS *i*	13.02	0.01	1.0×10^{-14}	44.3	Chambers et al. (2016)
Pan-STARRS *z*	12.50	0.01	1.3×10^{-14}	59.7	Chambers et al. (2016)
Pan-STARRS *y*	12.14	0.01	1.4×10^{-14}	75.7	Chambers et al. (2016)
2MASS *J*	10.81	0.02	1.3×10^{-14}	90.3	Skrutskie et al. (2006)
2MASS *H*	9.94	0.02	1.0×10^{-14}	98.1	Skrutskie et al. (2006)
2MASS K_s	9.69	0.02	4.9×10^{-15}	60.6	Skrutskie et al. (2006)
WISE *W1*	9.47	0.02	1.1×10^{-15}	21.5	Wright et al. (2010)
WISE *W2*	9.52	0.02	3.2×10^{-16}	8.6	Wright et al. (2010)
WISE *W3*	9.37	0.04	1.0×10^{-17}	0.7	Wright et al. (2010)
WISE *W4*	>8.29	2σ	$<2.2 \times 10^{-18}$	<0.3	Wright et al. (2010)

Table 5. Parameter estimates from the two-star SED model fit. We used model atmospheres with [M/H] = −0.5 and assumed a reddening of $E(B-V) = 0.54$.

Parameter	Companion	Giant
$T_{\rm eff}$ (K)	5000 ± 125	4000 ± 125
R (R$_\odot$)	11.1 ± 0.6	25.4 ± 1.4
L (L$_\odot$)	56 ± 6	148 ± 16

Figs 1 and 2 present the ASAS-SN, ATLAS, ZTF, and *TESS* light curves for 2M0412 phased at the orbital period of $P_{\rm orb} \simeq 81.2$ d. When phased with the orbital period, the light curves have two equal maxima and two unequal minima, which is typical of ellipsoidal variability. The light curves in the bluer filters tend to have more scatter than those in the redder filters. This is likely physical in nature and could indicate the presence of spots on the giant.

2.3 UV photometry

We obtained *Swift* UVOT (Roming et al. 2005) images in the *UVM2* (2246 Å) band (Poole et al. 2008) through the Target of Opportunity programme (Target ID number 14417). We only obtained images in the *UVM2* band because the *Swift UVW1* and *UVW2* filters have significant red leaks that make them unusable in the presence of the emission from the cool giant. Each epoch of UVOT data includes multiple observations, which we combined using the `uvotimsum` package. We then used `uvotsource` to extract source counts using a 5″.0 radius aperture centred on the star. We measured the background counts using a source-free region with a radius of 40″.0 and used the most recent calibrations (Poole et al. 2008; Breeveld et al. 2010) and taking into account the recent update to the sensitivity corrections for the *Swift UV* filters.[2] We were unable to detect 2M0412 in the *Swift UVM2* data. The *UVM2* observations are summarized in Table 1.

[2]https://www.swift.ac.uk/analysis/uvot/index.php

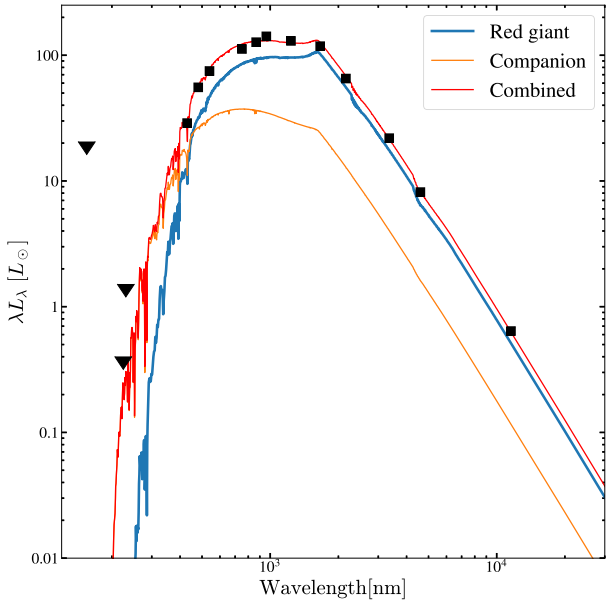

Figure 6. The best-fitting, extinction-corrected 2-star VOSA SED model for 2M0412. The multiband photometry for 2M0412 is shown in black. The *Swift UVM2* and *GALEX FUV/NUV* upper limits are shown as arrows. The observed SED is well fit with a composite SED of a red giant and subgiant binary.

2M0412 was previously observed as part of the *GALEX* Medium Imaging Survey (MIS) and All-Sky Imaging Survey (AIS) in 2011 January and 2004 January, respectively (Morrissey et al. 2007). As part of the MIS survey, 2M0412 was observed for 1689 s in the *NUV* filter. Additionally, 2M0412 was observed for 232 s in both the *NUV* and *FUV* filters. We do not detect 2M0412 in any of the *GALEX* images. In the *NUV*, we adopt the 22.7 AB mag 5σ upper limit from the longer MIS exposure (Bianchi, Conti & Shiao 2014). In the *FUV*, we adopt the 19.9 AB mag 5σ upper limit from the AIS exposure. The *GALEX* observations are summarized in Table 1.

2.4 Spectroscopic observations

To better sample the radial velocities, we obtained 10 additional spectra. These observations, along with the archival APOGEE DR16 observations, are summarized in Table 2. Using the HIRES instrument (Vogt et al. 1994) on Keck I, we obtained eight spectra with $R \approx 60000$ between 2021 August 14 and 2021 November 19 using the standard California Planet Search (CPS) set-up (Howard et al. 2010). The exposure times ranged from 292 to 515 s. We also obtained very high resolution ($R \approx 130\,000$) spectra on 2021 September 10 and 2021 October 2 using the Potsdam Echelle Polarimetric and Spectroscopic Instrument (PEPSI; Strassmeier et al. 2015) on the *Large Binocular Telescope*. We used the 200 µm fibre and two cross-dispersers (CD). The data were processed as described in Strassmeier, Ilyin & Steffen (2018). The total integration time for each epoch was 70 min, and the two CDs cover the wavelength ranges 4758–5416 Å and 6244–7427 Å. The HIRES, PEPSI, and MODS observations are summarized in Table 2.

2.5 X-ray data

We analysed the X-ray observations from the *Swift X-Ray Telescope* (*XRT*; Burrows et al. 2005) taken simultaneously with the *UVM2* observations. Individual exposure times ranged from 120 to 1650 s, for a total of 4010 s. All *XRT* observations were reprocessed using the *Swift* XRTPIPELINE version 0.13.2 and standard filter and screening criteria[3] and the most up-to-date calibration files. To increase the signal to noise of our observations, we combined all cleaned individual *XRT* observations using XSELECT version 2.4g. To place constraints on the presence of X-ray emission (see Section 3.5), we used a source region with a radius of 30 arcsec centred on the position of 2M0412 and a source-free background region with a radius of 150 arcsec located at RA = 04:12:38.10, Dec = 67:43:00.86 (J2000).

3 RESULTS

Here, we present our analyses of the observations described in Section 2. In Section 3.1, we fit Keplerian models to the radial velocities and derive an SB2 spectroscopic orbit for 2M0412. In Section 3.2, we characterize the red giant and its companion using its spectral energy distribution (SED) and spectra. In Section 3.3, we model the ellipsoidal variations of the red giant using multiband light curves and the binary modelling tool PHOEBE to derive the masses of the red giant and the companion. In Section 3.4, we discuss the broad Balmer Hα emission and its orbital phase dependent variability. In Section 3.5, we discuss the X-ray observations.

3.1 Keplerian orbit models

We fit Keplerian orbits to the APOGEE DR16, HIRES, and PEPSI radial velocities using two separate codes. First, we use `TheJoker` (Price-Whelan et al. 2017) Monte Carlo sampler. We first fit the joint data set using a broad uniform prior in period spanning [1 d,1000 d]. We obtain a unimodal solution at $P_{\rm orb} \simeq 82.6$ d, which is close to the orbital period from the light curves. We then reran `TheJoker` with a Gaussian prior on the period of $P_{\rm orb} = 81.2 \pm 0.5$ d. In these joint fits we also include additional parameters to allow for any velocity zero-point offsets between the three instruments and set the argument of periastron to $\omega = 0$ after confirming that there was no evidence for a non-zero ellipticity. The results of the fits are summarized in Table 3. The mass functions are well-constrained and mutually consistent, and the elliptical models yield a very small, non-zero ellipticity that is not significant. As a second, independent fit, we use the YORBIT genetic algorithm (Ségransan et al. 2011), frequently used in the discovery of extra-solar planets (e.g. Mortier et al. 2016; Martin et al. 2019). We find orbital parameters consistent with `TheJoker` results. In Fig. 3, we plot the YORBIT fit to the data. Given that the orbit is circular, we define the phase relative to the epoch of maximal radial velocity of the primary red giant $T_{\rm RV,max,primary} = 2457722.795 \pm 0.130$ d instead of the epoch of periastron. The ephemeris for $\phi = 0$ is $T_0 = 2457661.919 \pm 0.164$ d. We define orbital phases so that $T_{\rm RV,\,max,\,primary}$ corresponds to $\phi = 0.75$, the companion (secondary) and the giant (primary) would be eclipsed at $\phi = 0.5$ and $\phi = 0$, respectively, for an edge-on orbit.

The automated SB2 analysis tool `reamatch` (Kolbl et al. 2015) in the Keck CPS pipeline is used to identify double-lined spectroscopic binaries. `reamatch` looks for a library spectrum that minimizes a χ^2 fit to the observed spectrum. Once the best-fitting library spectrum for the primary is identified, it is subtracted from the data and the residuals are modelled to search for evidence of emission from a secondary star. `reamatch` finds evidence of a secondary for 2M0412 in most of the HIRES spectra. Fig. 4 shows the χ^2 as a function of the Doppler

[3] http://swift.gsfc.nasa.gov/analysis/xrt_swguide_v1_2.pdf

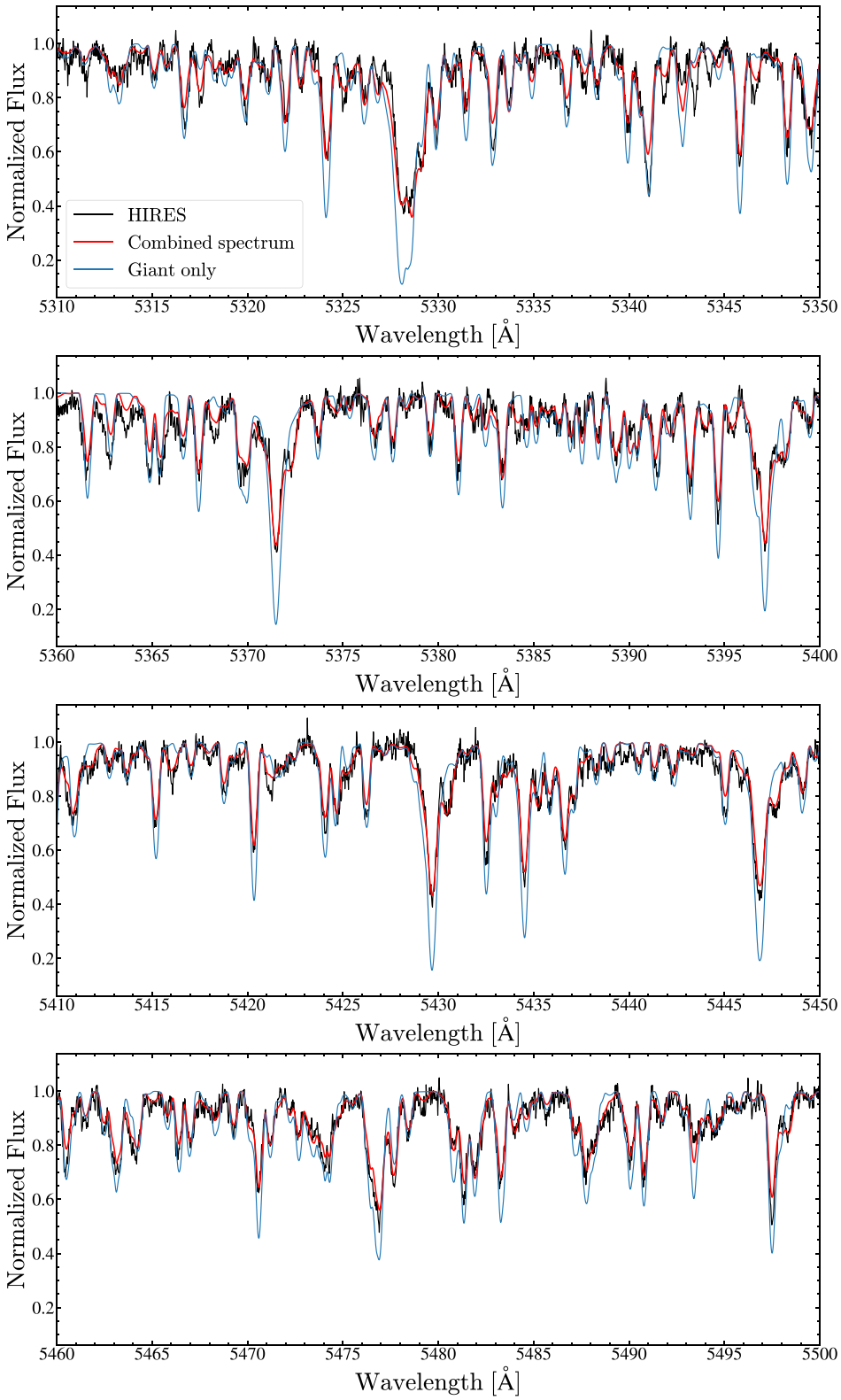

Figure 7. The Keck/HIRES spectrum (black) and the best-fitting composite spectrum (red) for a red giant + lower giant binary with $F_{\rm comp}/F_{\rm tot} = 0.35$. The spectrum of a single giant star is shown in blue. The composite spectrum fits the HIRES spectrum better than a single giant.

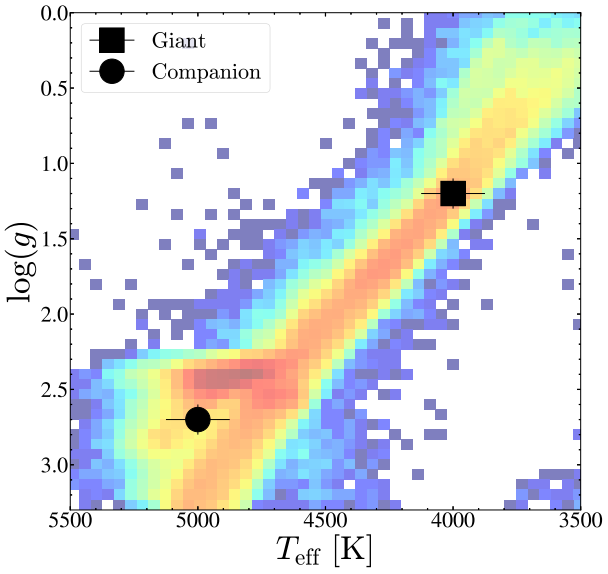

Figure 8. log (*g*) versus $T_{\rm eff}$ for the sample of APOGEE DR16 giants with $-1 < [{\rm M/H}] < 0$. The positions of the giant and the companion are shown in black.

shift for the HIRES epoch at phase 0.92. The dips are seen when the absorption lines in the observed spectra align with the Doppler shifted template spectrum. The presence of two dips in Fig. 4 suggests that two stars contribute to the observed HIRES spectrum. However, `reamatch` only reports an approximate velocity for the second component. To derive more precise estimates, we use `iSpec` to derive RVs for this second component for both the HIRES and PEPSI epochs by cross-correlating the spectra with a synthetic spectrum of a 4250 K red giant. RVs are derived by fitting two Gaussians to the cross-correlation function (CCF) computed by `iSpec`. `reamatch` also provides estimates of the secondary temperature and the relative brightness of the secondary in the *V*/*R* bands. The secondary temperature is estimated to be $T_{\rm eff,\,comp} \sim$ 6000–6100 K, which lies at the edge of the `reamatch` grid. Once the temperature of the secondary is estimated, `reamatch` estimates the brightness of the secondary relative to the primary. This is done through the injection of another spectrum into the original spectrum. This process is described in detail in Kolbl et al. (2015). The relative brightness of the secondary in 2M0412 is estimated to range from ∼20 to ∼75 per cent in the *V* and *R* bands. However, these estimates from `reamatch` are not reliable because the library spectra largely consist of main-sequence stars and template spectra for evolved giants are scarce.

Fig. 5 shows the radial velocities for the secondary component after subtracting the systemic velocity v_γ. If we fix the period and orbital phases based on the orbit of the primary giant, we find a good fit (see Fig. 5) to these velocities with $K_{\rm comp} = 8.3 \pm 0.1\,{\rm km\,s^{-1}}$, which implies $q = M_{\rm giant}/M_{\rm comp} = 0.201 \pm 0.010$ and $a_{\rm comp}\sin i = 13.3 \pm 0.2\,{\rm R_\odot}$. A synchronized, Roche lobe filling star satisfies the relation

$$v_{\rm rot} \sin i / K_{\rm giant} = 0.462\, q^{1/3}(1+q)^{2/3} \quad (2)$$

(see e.g. Wade & Horne 1988; Torres et al. 2002). With this relation, we obtain $q = 0.21 \pm 0.03$, which is entirely consistent with the mass ratio derived from the velocities. This indicates that the giant has likely filled its Roche lobe.

Using just the dynamical information ($K_{\rm giant}$, $K_{\rm comp}$, and $P_{\rm orb}$), we get $a_{\rm orb}\sin i = (a_{\rm giant} + a_{\rm comp})\sin i = 80.4 \pm 0.2\,{\rm R_\odot}$. Using Kepler's third law, this corresponds to $M_{\rm tot}\sin^3 i = (M_{\rm giant} + M_{\rm comp})\sin^3 i = 1.06 \pm 0.01\,{\rm M_\odot}$. Using the constraint on q, we can derive the minimum mass of the companion and the giant as

$$M_{\rm comp}\sin^3 i = 0.88 \pm 0.01\,{\rm M_\odot}, \quad (3)$$

and

$$M_{\rm giant}\sin^3 i = 0.18 \pm 0.01\,{\rm M_\odot}. \quad (4)$$

Table 6. PHOEBE parameter estimates for the red giant primary and secondary companion. The reported errors are purely statistical and do not include systematic effects.

Parameter	Companion	Giant
$P_{\rm orb}$ (d)	81.1643 (fixed)	
ω (°)	0 (fixed)	
e	0 (fixed)	
γ (km s^{-1})	−47.031 (fixed)	
a (R$_\odot$)	$17.4^{+0.1}_{-0.1}$	$86.7^{+0.5}_{-0.4}$
i (°)	$49.44^{+0.31}_{-0.36}$	
$T_{\rm eff}$ (K)	5000 (fixed)	4000 (fixed)
R (R$_\odot$)	11.1 (fixed)	26.1 ± 0.1
q	0.201 (fixed)	
M (M$_\odot$)	1.91 ± 0.03	0.38 ± 0.01
log (g)	2.64 ± 0.01	1.19 ± 0.01

3.2 Properties of the primary red giant and its companion

3.2.1 Modelling the SED

We characterized the primary red giant and the secondary companion using both fits to its overall SED and analyses of the available spectra. For the SED, we used photometry from APASS DR10 (Henden et al. 2018), Pan-STARRS DR1 (Chambers et al. 2016), 2MASS (Skrutskie et al. 2006), and AllWISE (Wright et al. 2010). We used the *Swift UVM2* and *GALEX NUV* photometry as upper limits. The compilation of the multiband photometry used in these fits is given in Table 4.

We initially fit single-star models to the SED of 2M0412 using DUSTY (Ivezic & Elitzur 1997; Elitzur & Ivezić 2001) inside a MCMC wrapper (Adams & Kochanek 2015). We assumed only foreground extinction due to $R_V = 3.1$ dust (Cardelli, Clayton & Mathis 1989) and used the ATLAS9 (Castelli & Kurucz 2003) model atmospheres for the star. We assume that the source is at a distance of 3.7 kpc and used minimum luminosity uncertainties of 10 per cent for each band to compensate for any systematic errors and for the observed variability. We used a temperature prior based on APOGEE DR16 of $T_{\rm eff,\,giant} = 4188 \pm 75$ K and a prior of $E(B-V) = 0.54 \pm 0.10$ on the extinction from `mwdust` (Drimmel, Cabrera-Lavers & López-Corredoira 2003; Marshall et al. 2006; Bovy et al. 2016; Green et al. 2019). Ignoring the upper limits, we are fitting 11 photometric bands with three variables (L_*, T_*, and $E(B-V)$) and two priors, leading to a best fit with $\chi^2 = 3.8$ for 10 degrees of freedom. The single-star SED fit yields $T_{\rm eff,\,giant} \simeq 4207 \pm 68$ K, $L_{\rm giant} = 196 \pm 15\,{\rm L_\odot}$, $R_{\rm giant} \simeq 26.4 \pm 0.6\,{\rm R_\odot}$, and $E(B-V) = 0.587 \pm 0.046$ mag.

However, given that we detect a second component in the CCF, we use `VOSA` (Bayo et al. 2008) and the ATLAS9 (Castelli & Kurucz 2003) model atmospheres to fit the SED of 2M0412 using a binary star model. We keep the reddening fixed at $E(B-V) = 0.54$ and assume a metallicity of [M/H] = −0.5 based on the fits to the spectra in Section 3.2.2. We obtain a good fit to the data using `VOSA` and obtain $T_{\rm eff,\,giant} \simeq 4000 \pm 125$ K, $L_{\rm giant} = 148 \pm 16\,{\rm L_\odot}$, $R_{\rm giant} \simeq$

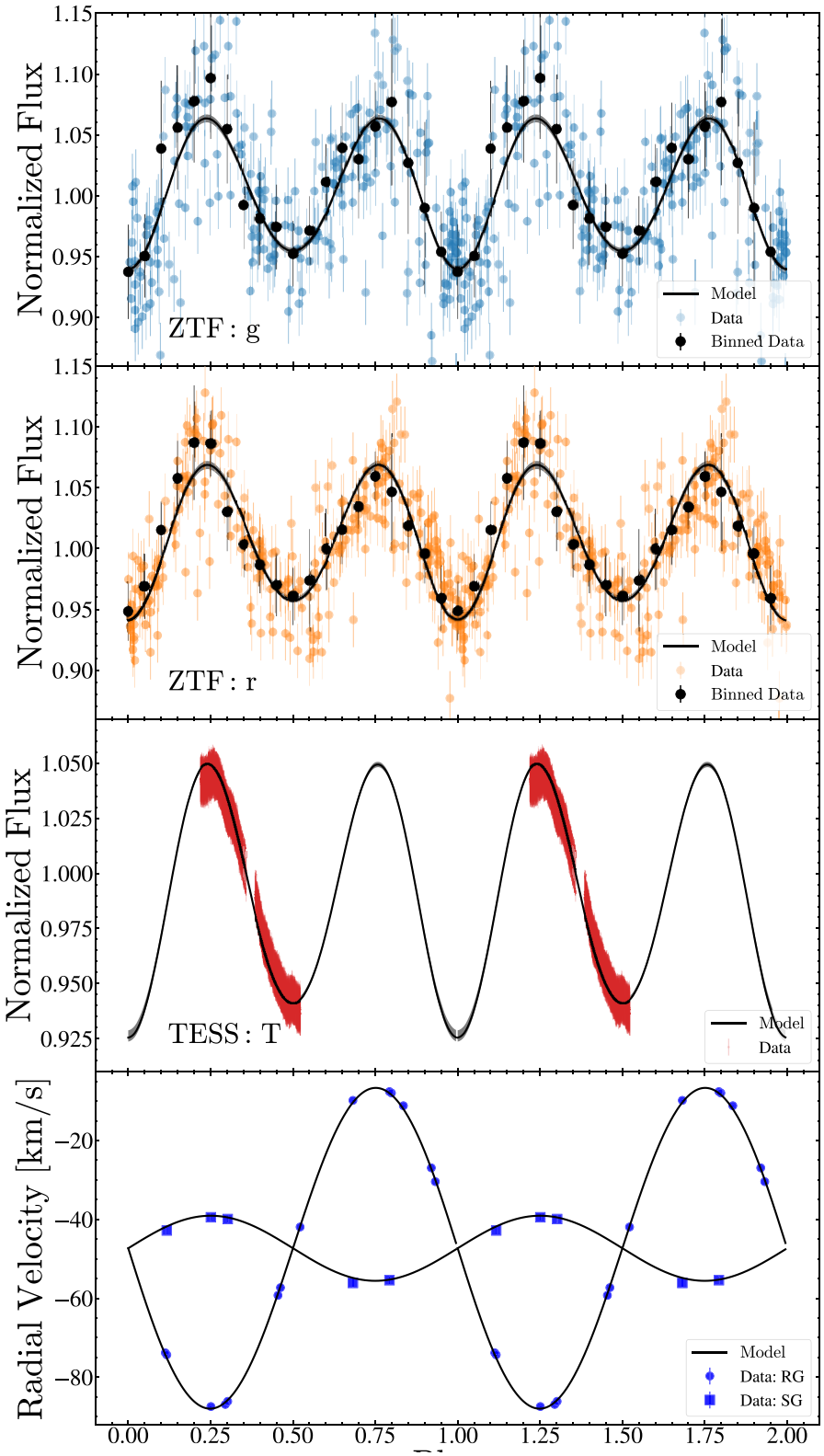

Figure 9. The normalized ZTF *g*-, ZTF *r*-, and *TESS T*-band light curves for 2M0412 as a function of orbital phase (defined with the epoch of maximal RV at $\phi = 0.75$). The binned light curves for the ZTF *g*- and ZTF *r*-band light curves are shown as black points. The scatters in the bins are shown as error bars. The light curves and RV curves from the best-fitting PHOEBE model are also shown.

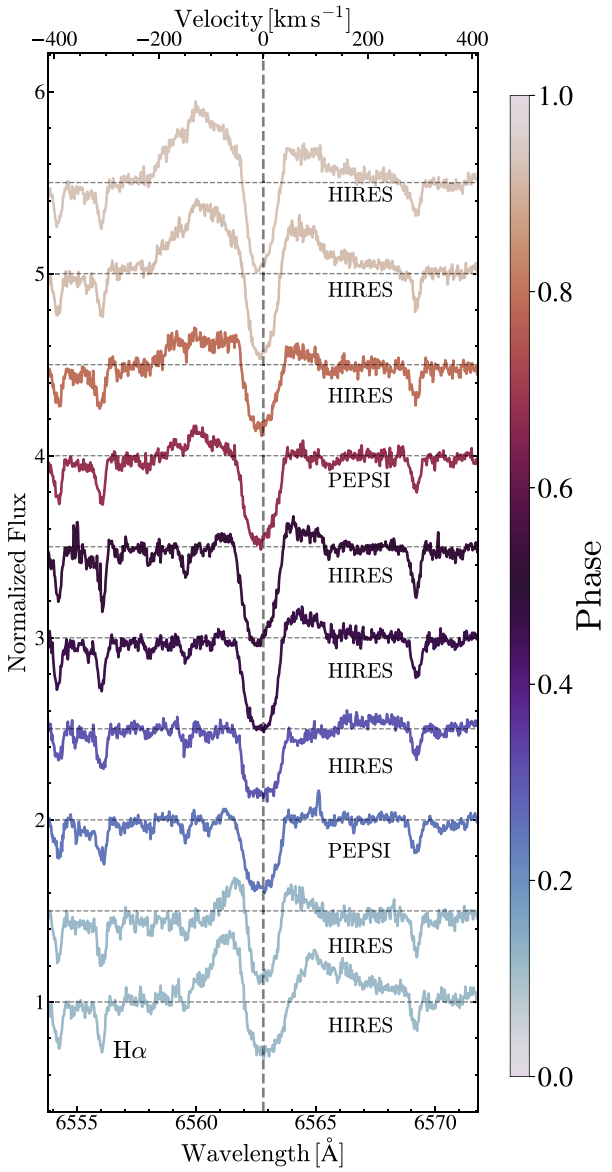

Figure 10. H α line profiles in the rest frame of the giant in the HIRES and PEPSI spectra. The line profiles are sorted and coloured as a function of orbital phase.

$25.4 \pm 1.4\,R_\odot$, $T_{\rm eff,\,comp} \simeq 5000 \pm 125$ K, $L_{\rm comp} = 56 \pm 6\,L_\odot$, and $R_{\rm comp} \simeq 11.1 \pm 0.6\,R_\odot$ (Table 5). We are fitting 13 photometric bands with three variables ($L_{\rm giant}$, $L_{\rm comp}$, $T_{\rm eff,\,giant}$, and $T_{\rm eff,\,comp}$), leading to a best fit with $\chi^2 = 41.1$ for 12 degrees of freedom. The two-star SED model indicates that if the companion is stellar, it is a giant located on the lower red giant branch.

3.2.2 Modelling the HIRES/PEPSI spectra

The APOGEE, HIRES, and PEPSI spectra indicate that the giant is rapidly rotating. The APOGEE DR16 spectra were used to measure $v_{\rm rot} \sin i = 12.61 \pm 0.92\,{\rm km\,s^{-1}}$ following the methods described in Tayar et al. (2015), Dixon, Tayar & Stassun (2020), and Mazzola Daher et al. (2022). The HIRES CPS pipeline (Petigura 2015) reports $v_{\rm rot} \sin i = 13.3 \pm 1.0\,{\rm km\,s^{-1}}$ and we found $v_{\rm rot} \sin i = 12.8 \pm 1.2\,{\rm km\,s^{-1}}$ from the PEPSI spectrum using `iSpec` (Blanco-Cuaresma et al. 2014; Blanco-Cuaresma 2019).

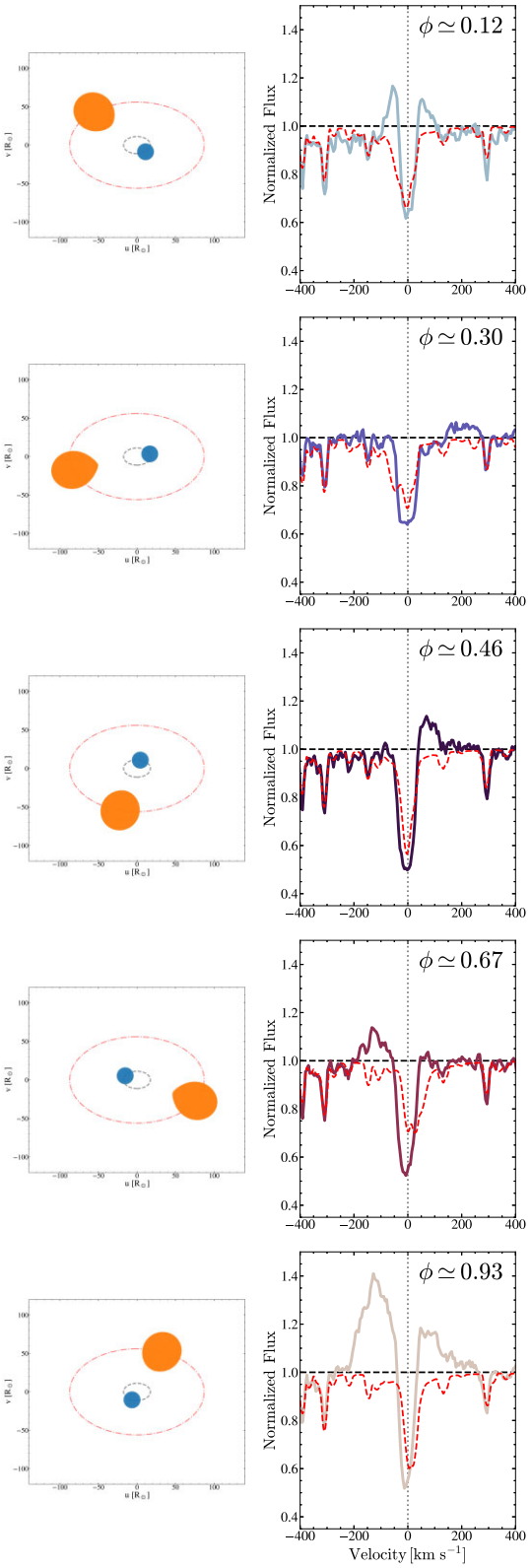

Figure 11. Behaviour of the H α line profiles with orbital phase. The right panels show the H α line profiles at the orbital configurations illustrated in the left-hand panels. The red dashed line shows the synthetic composite spectrum for the binary at the corresponding orbital phase.

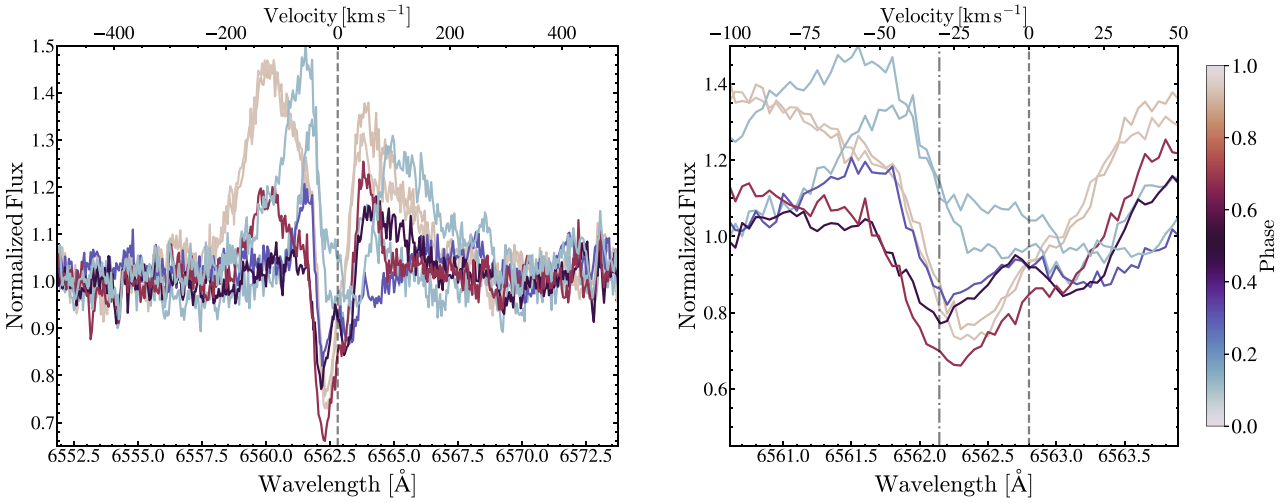

Figure 12. Variations of the Hα line profiles with orbital phase in the giant's rest frame after subtracting a template composite spectrum for the binary. The left-hand panel shows the full wavelength range and the right-hand panel zooms in on the line core. Note the Hα absorption feature at $\simeq$–30 km s^{-1} in the giant's rest frame.

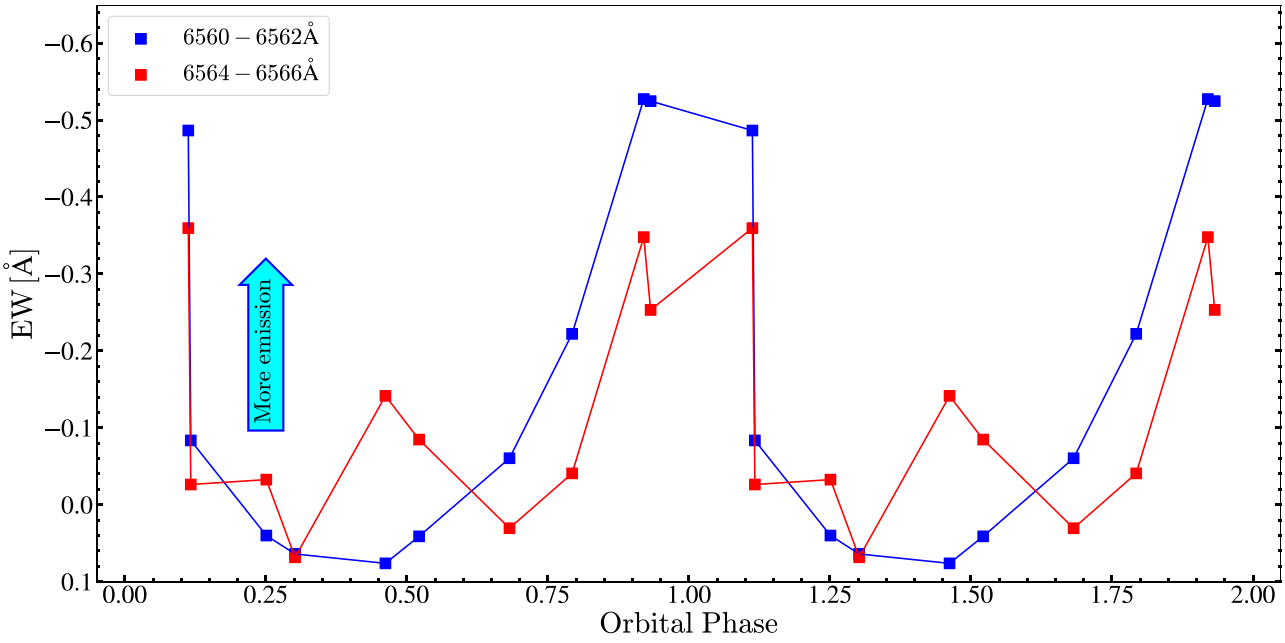

Figure 13. Equivalent width of the blue-shifted (blue points, 6560–6562 Å) and red-shifted (red points, 6564–6566 Å) Hα emission components as a function of orbital phase.

Assuming that the rotation of the giant is tidally synchronized with the orbit, we can derive the rotational velocity

$$v_{\rm rot} = \frac{2\pi R_{\rm giant}}{P_{\rm rot}} = 15.6 \pm 0.4\,{\rm km\,s^{-1}} \left(\frac{R_{\rm giant}}{25\,{\rm R_\odot}}\right) \quad (5)$$

for the giant. This is a reasonable assumption because binaries with evolved components [$\log(g) < 2.5$] and orbital periods shorter than $\sim$100 d are expected to be tidally locked (e.g. Verbunt & Phinney 1995; Price-Whelan & Goodman 2018). However, the light-curve residuals after removing the ellipsoidal variability show no periodic signal that might confirm or reject this hypothesis. The APOGEE DR16, HIRES, and PEPSI measurements combined with the period and stellar radius yield estimates of $\sin i = 0.80 \pm 0.05$, $\sin i = 0.85 \pm 0.05$, and $\sin i = 0.82 \pm 0.06$, respectively, and orbital inclinations of $i = 53.1 \pm 3.9°$, $i = 58.2 \pm 4.1°$, and $i = 55.1 \pm 4.7°$, respectively. To investigate the rotation of the second component, we subtract a synthetic spectrum of the giant from the HIRES spectra and shift the residuals to the companion's rest frame. We then calculate the median spectrum from these residuals and measured $v_{\rm rot} \sin i = 17.6 \pm 0.6$ km s^{-1} for the companion.

We use the spectral synthesis code `iSpec` to synthesize spectra for a giant with $T_{\rm eff,\,giant} \simeq 4000$ K, $\log(g)_{\rm giant} \simeq 1.2$, and a lower giant with $T_{\rm eff,\,comp} \simeq 5000$ K and $\log(g)_{\rm comp} \simeq 2.7$ for a metallicity of [Fe/H] = −0.5 using MARCS model atmospheres (Gustafsson et al. 2008). Our two-star SED model indicates that the lower giant secondary companion contributes $\sim$35 per cent of the total flux in the V band between 530–550 nm, so we kept the flux ratio fixed

Table 7. Properties of exemplary BPASS giant + star binary models that match observations for 2M0412.

Model	M_1 ($M_\odot$)	M_2 ($M_\odot$)	$P_{\rm orb,\ init}$ (d)	$M_{\rm giant}$ ($M_\odot$)	$M_{\rm He\ core}$ ($M_\odot$)	$M_{\rm comp}$ ($M_\odot$)	q	$T_{\rm eff,\ giant}$ (K)	$T_{\rm eff,\ comp}$ (K)	$R_{\rm giant}$ ($R_\odot$)	$R_{\rm comp}$ ($R_\odot$)	$L_{\rm giant}$ ($L_\odot$)	$P_{\rm orb}$ (d)	Age Gyr
1	1.5	0.9	10.0	0.41	0.34	2.30	0.176	4078	6353	27.8	2.1	191	79.3	2.2
2	1.4	0.9	10.0	0.37	0.33	2.14	0.173	4101	6037	27.5	2.1	193	82.9	2.7
3	1.7	0.7	15.9	0.35[a]	0.33	1.55	0.227	4279	6489	26.7	1.4	215	82.0	1.5

Note.
[a]Best matching giant + star model.

at $F_{\rm comp}/F_{\rm tot} = 0.35$ for this wavelength range. We assumed an α-enhancement of $[\alpha/{\rm Fe}] = 0.2$. The spectra were broadened based on our $v_{\rm rot} \sin i$ measurements for the giant and the companion. We shifted the spectrum of the companion based on the derived velocities and then combined the two spectra using the flux ratio indicated by the binary SED model. Fig. 7 shows the combined synthetic spectrum and the observed HIRES spectrum at phase $\phi \simeq 0.68$. The combined spectrum (Fig. 7) is a very good fit to the data. We also note that the spectrum of a giant without additional veiling and absorption lines from a companion cannot fit the data as well as the combined model.

Fig. 8 shows the position of the giant and the companion in $\log(g)$ versus $T_{\rm eff}$. Both the giant and the companion have $T_{\rm eff}$ and $\log(g)$ that agree with the distribution of APOGEE DR16 sources. In DR16, 2M0412 has $T_{\rm eff} = 4187 \pm 75$, $\log(g) = 1.80 \pm 0.06$, and $[{\rm Fe/H}] = -0.73 \pm 0.01$. The measured value of $\log(g)$ in DR16 is somewhat larger than our estimate. However, the APOGEE ASPCAP pipeline routinely overestimates $\log(g)$ for rapidly rotating giants because the ASPCAP template library of synthetic spectra does not include rotation for giants. For giants rotating at $v_{\rm rot} \sin i \sim 8 - 14\,{\rm km\,s^{-1}}$, the offset in $\log(g)$ can be as large as 0.1–0.5 dex (see e.g. Thompson et al. 2019). This bias can also affect other spectroscopically determined parameters for these rapidly rotating stars. Given that the secondary companion contributes ∼20 per cent of the light in the APOGEE spectra, the single star ASPCAP fits will also yield biased results. El-Badry et al. (2022b) presents binary fits to the APOGEE spectra that are consistent with our results from fitting the spectra with a two-star model.

3.3 Modelling the ellipsoidal variability with PHOEBE

We interpret the light curves as ellipsoidal variability and fit models to derive the orbital properties and dynamical masses of the red giant and its companion.

We tried MCMC fits of the ZTF *g*-band, *r*-band, and *TESS* light curves using `PHOEBE` (Foreman-Mackey et al. 2013; Prša et al. 2016; Horvat et al. 2018; Conroy et al. 2020) with priors on the radius ($R_{\rm giant} = 25.4 \pm 1.5 R_\odot$). We do not consider the effects of irradiation and reflection in our models. We adopt a logarithmic limb-darkening law and use coefficients from Claret & Bloemen (2011) and Claret (2017). We fixed the orbital parameters to those obtained from `yorbit` (Table 3) and kept the mass ratio fixed at $q = 0.201$. Initial models suggested that the giant was close to filling its Roche lobe and spectroscopic evidence for an accretion disc provides additional support for the argument that the giant is filling its Roche lobe (see Section 3.4), so we constrained the giant to be semidetached. We keep the radius of the companion and the temperatures fixed at $R_{\rm comp} \simeq 11.1 R_\odot$, $T_{\rm eff,\ giant} = 4000$ K, and $T_{\rm eff,\ comp} = 5000$ K. We fit for the orbital inclination (i), and the radius of the giant ($R_{\rm giant}$). We marginalize over the passband luminosities and nuisance parameters that account for underestimated errors in the light curves.

Table 6 presents the results of our best-fitting `PHOEBE` model. The reported errors are purely statistical and are likely an underestimate of the true uncertainty in the model. This is because we do not consider systematic effects in the derivation of the binary solution. The mass of the giant is $M_{\rm giant} = 0.38^{+0.01}_{-0.01}\,M_\odot$, the radius of the giant is $R_{\rm giant} = 26.1 \pm 0.1\,R_\odot$, and the orbital inclination is $i_{\rm orb} = 49.44^{+0.31\circ}_{-0.36}$. The radius of the giant derived from the `PHOEBE` model is consistent with that obtained from the two-star SED model in Section 3.2 (Table 5). The inferred mass of the red giant ($M_{\rm giant} \simeq 0.38\,M_\odot$) is inconsistent with single-star evolution and instead implies that it has been heavily stripped by binary interaction. In this model, the companion mass is $M_{\rm comp} = 1.91^{+0.03}_{-0.03}\,M_\odot$. This model is a good fit to the ZTF *g*-band, *r*-band, the *TESS T*-band light curve, and the radial velocities (Fig. 9). The masses and luminosities (Table 5) of the giant and its companion imply that 2M0412 is an Algol-type binary that has undergone mass transfer, where the more luminous star is also the least massive.

3.4 Balmer H α emission

As shown in Fig. 10, there is a broad H α emission line whose structure varies with the orbital phase. V723 Mon also has this property (Jayasinghe et al. 2021b), but here it is directly visible without any need to subtract the stellar spectrum.

We identify both blue-shifted and red-shifted emission components in most of our spectra. We define these components by the wavelength ranges of 6560–6562 Å and 6564–6566 Å, respectively. The most significant H α emission in our spectra is seen near phase $\phi \sim 0.9$ as a blue-shifted component. The emission component has a velocity close to the rest frame of the giant near phase $\phi \sim 0.25$ and fills in the giant's H α absorption line. Near phase ∼0.9, the typical Gaussian full width at half-maximum (FWHM) of the blue-shifted (red-shifted) H α emission component is $\sim 255\,{\rm km\,s^{-1}}$ ($\sim 265\,{\rm km\,s^{-1}}$). The wings of the emission extend beyond $\sim 200\,{\rm km\,s^{-1}}$ in some of our spectra.

The peak separations at $\phi \sim 0.1$ and $\phi \sim 0.9$ are ∼160 and $\sim 196\,{\rm km\,s^{-1}}$, respectively. However, the behaviour of the double-peaked profile appears to vary between orbits. For example, we obtained Keck/HIRES spectra near $\phi \sim 0.1$ in two consecutive orbits, where the first spectrum has a peak separation of $\sim 106\,{\rm km\,s^{-1}}$ and the second spectrum has a much larger peak separation of $\sim 160\,{\rm km\,s^{-1}}$. For the epochs where we can see a double-peaked emission profile, the median peak separation is $\sim 168\,{\rm km\,s^{-1}}$ with a scatter of $\sigma \sim 31\,{\rm km\,s^{-1}}$.

Fig. 11 shows the H α line at various orbital phases along with the `PHOEBE` models of the orbital configurations of the binary. After conjunction at $\phi \simeq 0.5$, the emission is blue-shifted and reaches a maximum at phase $\phi \sim 0/1$ (Fig. 13). Since the H α emission varies significantly in the rest frame of the giant, this emission must emerge from beyond the giant's photosphere. Given its large FWHM, we can

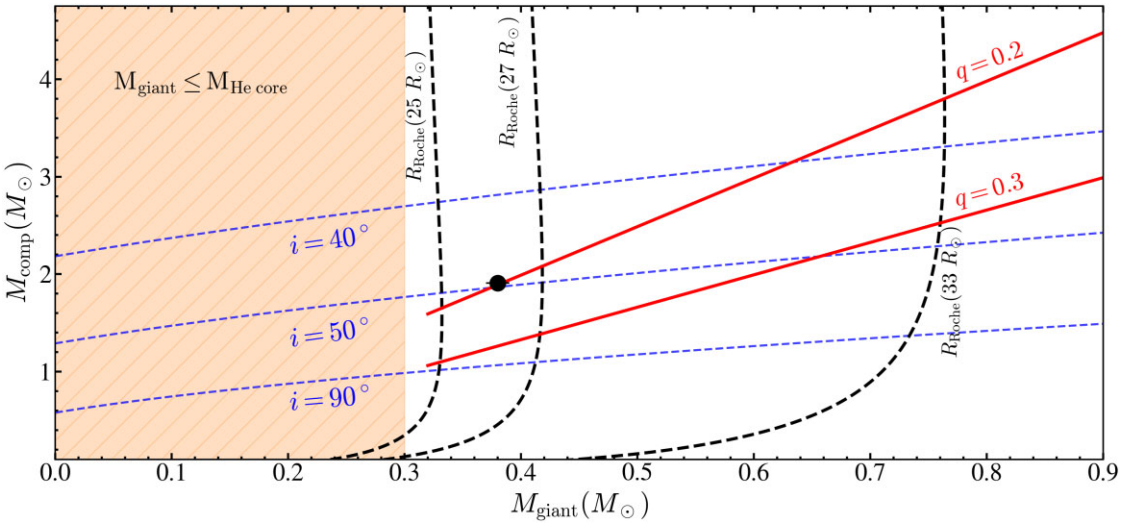

Figure 14. The mass of the companion ($M_{\rm comp}$) as a function of the mass of the giant ($M_{\rm giant}$). The binary mass function at inclinations of $i = 90^\circ$, 50°, and 40° are shown as the blue dashed lines. Giants with radii of $R = 25$ R$_\odot$, $R = 29$ R$_\odot$, or $R = 33$ R$_\odot$ will overfill their Roche lobes of $R_{\rm Roche}(R)$ if they have masses less than the Roche limits given by the dashed curves. The companion masses for a mass ratio of $q = 0.2$ and $q = 0.3$ are shown as the red lines. The orange shaded region highlights giant masses that are not allowed by the condition $M_{\rm giant} \gtrsim M_{\rm core} \simeq 0.32$ M$_\odot$ (equation 6). The derived values for $M_{\rm comp}$ and $M_{\rm giant}$ from the PHOEBE model (Section 3.3) are shown in black.

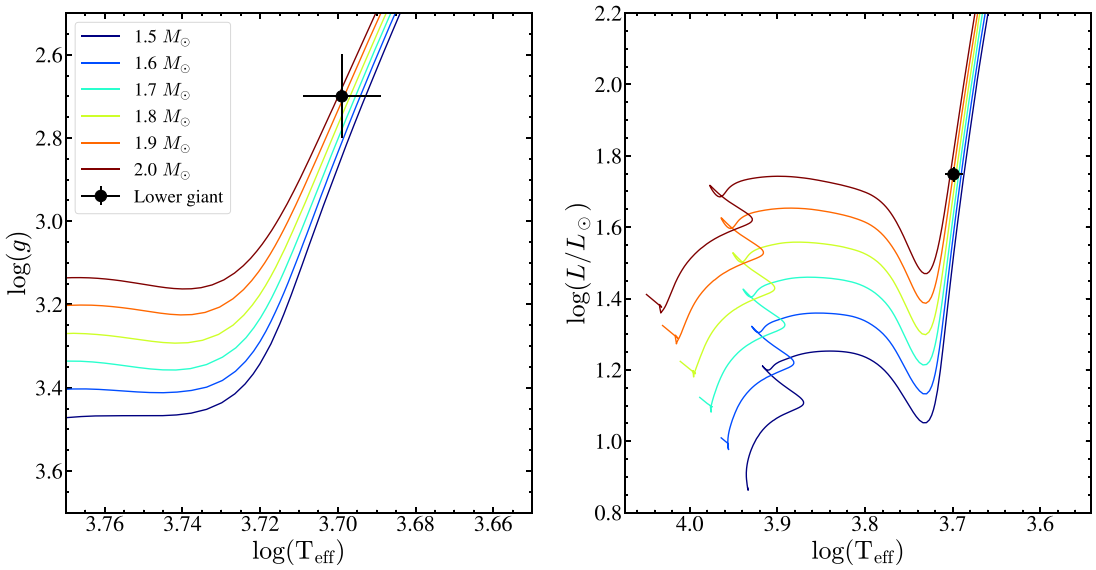

Figure 15. Left-hand panel: $\log(g)$ versus $T_{\rm eff}$ and, right-hand panel: $\log(L)$ versus $\log(T_{\rm eff})$. The position of the companion to 2M0412 is shown in black. MIST (Choi et al. 2016; Dotter 2016) stellar tracks for [Fe/H] $= -0.5$ are shown.

rule out a chromospheric origin for the H$\,\alpha$ emission. We also do not observe the Ca II H and K emission lines that are typically associated with chromospheric activity.

Fig. 12 shows the H$\,\alpha$ line profiles after subtracting the template spectrum of the red giant. We see a blue-shifted H$\,\alpha$ absorption feature in these line profiles at a roughly constant $\sim$30 km s^{-1} blue shift relative to the giant. The depth of the absorption core is strongest near $\phi \sim 0.5$. The velocity of this absorption feature is close to the velocity of the giant's photosphere ($v_{\rm rot,giant} \simeq 16$ km s^{-1}), consistent with mass outflow from the giant at L_1. At $\phi = 0$, the inner Lagrangian point (L_1) is directed toward the observer and at $\phi = 0.5$, L_1 points away from the observer (Beech 1985). It is possible that the absorption feature is associated with the companion or density enhancements caused by matter streaming through the inner Lagrangian point.

Fig. 13 shows how the equivalent width varies with orbital phase for both the blue-shifted and red-shifted H$\,\alpha$ components. The largest equivalent width of the blue-shifted (red-shifted) H$\,\alpha$ component is EW(H$\,\alpha$) ~ -0.5 (EW(H$\,\alpha$) ~ -0.3) at $\phi \sim 0.9$. These equivalent widths are more than an order of magnitude smaller than those observed for X-ray binaries (see e.g. Fender et al. 2009) and correspond to a total line luminosity of $\sim$0.003 L$_\odot$. For both the blue and red components, the equivalent widths are the most negative (emission is strongest) near $\phi \sim 0$ when the companion is on the near side of the giant. The red-shifted line also has a weaker peak at $\phi \sim 0.5$ when the companion is on the far side.

If we interpret the double peaked structure as an accretion disc, the projected radial velocity of the outer rim of an accretion disc is approximately equivalent to half the velocity separation of the two peaks V_h (see e.g. Smak 1981; Strader et al. 2015). In this case, the V_h of 84 km s^{-1} is significantly larger than the radial velocity semi-amplitude of the red giant (∼42 km s^{-1}). It is also slightly larger than the circular velocity at the surface of the giant (∼78 km s^{-1} for $M = 1$ M$_\odot$ and $R = 31$ R$_\odot$). Indeed, V_h is expected to be larger than the radial velocity semi-amplitude of the giant for classical Keplerian discs (see e.g. Paczynski 1977; Orosz et al. 1994).

In summary, we observe a phase-dependent, broad ($\gtrsim$200 km s^{-1}) Hα emission line in our spectra of 2M0412. We show that the morphology and orbital evolution of the Hα emission is likely due to an accretion disc. This is consistent with the red giant filling its Roche lobe. However, more spectra are needed to study the behaviour of the Hα emission in greater detail.

3.5 X-ray upper limit

No X-rays were detected in the *Swift XRT* observations. We derived a 3σ upper limit using the reprocessed observations of sw00014417001 (∼2.2 ks), a 50 arcsec source region centred on the source and a 150 arcsec source-free background region located at (α_{J2000}, δ_{J2000}) = (04:12:38.10,67:43:00.86). We derive an aperture corrected 3σ upper limit on the 0.3–2.0 keV count rate of 8.1×10^{-4} counts per s. Using the Galactic column density along the line of sight ($N_H \sim 1.34 \times 10^{22}$ cm^{-2}, HI4PI Collaboration et al. 2016), and an absorbed power law with a photon index of 2, we derive an absorbed (unabsorbed) flux of 1.7×10^{-14} erg cm^{-2} s^{-1} (5.0×10^{-14} erg cm^{-2} s^{-1}), which corresponds to an absorbed (unabsorbed) X-ray luminosity of 2.9×10^{31} erg s^{-1} (8.1×10^{31} erg s^{-1}). The *Swift XRT* limit on the X-ray luminosity is comparable to the $L_X \sim 10^{30}$–10^{31} ergs s^{-1} observed for quiescent X-ray binaries (Dinçer et al. 2018) and the $L_X \sim 10^{29}$–10^{30} ergs s^{-1} observed for chromospherically active RS CVn systems (Demircan 1987).

4 COMPARISON TO BINARY EVOLUTION MODELS

We used `hoki` (Stevance, Eldridge & Stanway 2020; Stevance, Parsons & Eldridge 2022) to search for Binary Population And Spectral Synthesis (BPASS, Eldridge et al. 2017; Stanway & Eldridge 2018) binary models consistent with the observed properties of 2M0412. We used the BPASS v2.2.1 models at $Z = 0.006$, which is the closest match to the metallicity derived in Section 3.2.

We restrict our search to models with:

(i) Period of the binary, $P_{\rm orb} = 81 \pm 8$ d,
(ii) $V = -0.6 \pm 1$ mag,
(iii) $J = -2.8 \pm 1$ mag,
(iv) $K = -3.5 \pm 1$ mag,
(v) Total luminosity of the binary, $\log(L_{\rm binary}) = 2.31 \pm 0.05$,
(vi) Radius of the giant, $\log(R_{\rm giant}) = 1.40 \pm 0.05$,
(vii) Effective temperature of the giant, $\log(T_{\rm eff}) = 3.60 \pm 0.05$,
(viii) Mass of the giant, $M_{\rm giant} = [0.25, 2]$ M$_\odot$, and
(ix) Binary mass ratio, $0.15 < q < 0.35$.

We searched for models where either (i) the companion is a star with an effective temperature lower than $T_{\rm eff,\,comp} < 7000$ K, or (ii) the companion is a compact object (i.e. a neutron star or a BH). We found 16 giant + star and 21 giant + compact object models that satisfied these criteria. The existence of numerous giant + compact object binary models in BPASS suggests that the parameter space in which 2M0412 currently exists is viable for the discovery of compact objects, though the detection of a luminous secondary leads us to reject a compact object model for 2M0412. In all of the BPASS models, the giant is heavily stripped with masses in the range of ∼0.35–0.46 M$_\odot$ ($M_{\rm init} \simeq$ 1.2–1.8 M$_\odot$) and ∼0.35–0.79 M$_\odot$ ($M_{\rm init} \simeq$ 0.9–2.5 M$_\odot$) for the giant + star and the giant + compact object models, respectively. Table 7 gives three examples of the giant + star binary models closest in period and magnitude [$P_{\rm orb} = 81 \pm 2$ d, $\Delta(M) = 0.5$ mag] to the observations.

The giant + star binary that best matches our data has $M_{\rm giant} \simeq 0.35$ M$_\odot$, $M_{\rm comp} \simeq 1.55$ M$_\odot$, $q \simeq 0.227$, $R_{\rm giant} \simeq 26.7$ R$_\odot$, and $T_{\rm eff,giant} \simeq 4279$ K. The current configuration of the giant + star binary is short-lived, with the orbit expanding to a period of ∼85.7 d in ∼2.4 Myr. In this model, the binary is undergoing RLOF for a total of ∼24 Myr. The two other giant + star binary models in Table 7 have similar properties. In these models, the giant loses ∼70–80 per cent of its initial mass. For a conservative mass-transfer binary, the accretor is spun up and will therefore be rapidly rotating. This is inconsistent with the rotation measured for the companion ($v_{\rm rot} \sin i = 17.6 \pm 0.6$ km s^{-1}). The companion to the giant is a main-sequence star that is ∼3–4 mag fainter than the overall binary in the V band. This is inconsistent with our model for this binary, where the companion is a lower giant that contributes significantly in the V band (∼35 per cent).

We were puzzled by (in particular) the low temperatures of the stellar companions in the BPASS models. The cause is that the present BPASS models only evolve one star at a time for reasons of speed (Eldridge & Stanway 2016). This can lead to misestimates of the properties of the accreting star (Eldridge, private communication). To examine this, we evolved the BPASS giant + star binaries (Table 7) using Modules for Experiments in Stellar Astrophysics (MESA; Paxton et al. 2011, 2013, 2015, 2018, 2019). MESA computes Roche lobe radii in binary systems using the fit of Eggleton (1983), and the mass transfer rates in Roche lobe overflowing binary systems are determined following the prescription of Kolb & Ritter (1990). We adopt the explicit mass-transfer calculation scheme in MESA.

We use the initial component masses and orbital periods from the BPASS models (see Table 7) to evolve the binaries, and we examine their properties when the binary has a period of $P_{\rm orb} \sim 81$ d. As in the BPASS models, the initially more massive component becomes a red giant with $M_{\rm giant} \simeq$ 0.32–0.34 M$_\odot$ and its companion is a main-sequence star with $M_{\rm comp} \simeq$ 1.6–2.1 M$_\odot$. In the MESA models, however, the companion to the giant is a hot, luminous main-sequence star with $T_{\rm eff,comp} \simeq$ 10 700–11 200 K, $R_{\rm comp} \simeq$ 1.4–1.6 R$_\odot$, $\log(g) \simeq 4.4$ and $L_{\rm comp} \simeq$ 24–28 L$_\odot$. Such a hot companion is grossly incompatible with the *NUV* limits from *Swift* and *GALEX* (Section 3.2, Fig. 6). This is also significantly hotter than the temperature derived for the companion from fitting the SED and the spectra ($T_{\rm eff,\,comp} = 5000 \pm 125$ K). The higher temperatures in the `MESA` models would make the companion easily visible. For the companion to be a lower giant with $T_{\rm eff,\,comp} \simeq 5000$ K, the initial configuration of the binary has to be more finely tuned than the BPASS models that we have explored in this work, such that the secondary is already leaving the main sequence when mass transfer begins. A detailed exploration of such MESA models is presented in El-Badry et al. (2022b).

5 DISCUSSION

In this section, we systematically discuss the nature of the companion given the observed properties of the system and the modelling results from Section 3.

Fig. 14 summarizes the overall landscape of the constraints on the masses of the giant and the companion. There are several constraints on the giant mass that are independent of single star evolution models and that we show in Fig. 14. First, the giant is on the upper RGB and not on the red clump (Fig. 8), so it has a degenerate core. The luminosity of a solar metallicity giant with a degenerate core of mass $M_{\rm core}$ is (Boothroyd & Sackmann 1988)

$$\left(\frac{L}{\rm L_\odot}\right) \approx 1170 \left(\frac{M_{\rm core}}{0.4\ \rm M_\odot}\right)^7, \quad (6)$$

so we must have $M_{\rm giant} > M_{\rm core} \simeq 0.30\ \rm M_\odot$ for $L \sim 150\ \rm L_\odot$. The core mass–luminosity relationship is weakly dependent on metallicity. For example, this limit changes to $M_{\rm giant} > M_{\rm core} \simeq 0.32\ \rm M_\odot$ for a metal-poor giant with $Z = 0.001$. This region is denoted by the orange hatched region in Fig. 14. Using the Eggleton (1983) approximation for the Roche limit we illustrate the Roche radii for 25, 27, and 33 $\rm R_\odot$ with the black dashed lines. We see in Fig. 14 that the giant must be more massive than $M_{\rm giant} \gtrsim 0.32\ \rm M_\odot$ for the radius of $R_{\rm giant} \simeq 25\ \rm R_\odot$ from the SED (Section 3.2). Note that this limit is identical to the argument that the mean density of a Roche lobe-filling star is largely determined by the period (Eggleton 1983), which was recently used by El-Badry & Burdge (2022) in arguing against the NGC 1850 BH1 candidate discussed in the introduction. For $q \simeq 0.2$ (Fig. 5), the giant's mass is $M_{\rm giant} \simeq 0.4\ \rm M_\odot$ and the companion has $M_{\rm comp} \simeq 1.9\ \rm M_\odot$ for $i \simeq 50^\circ$. This model is shown as the large filled black circle in Fig. 14.

While it is unlikely in the case of 2M0412, we investigated whether the second set of absorption lines could emerge from an accretion disc/flow surrounding a compact object. In Section 3.4, we show that the source has a broad, double-peaked H α emission line in our spectra, and argue that it likely emerges due to an accretion disc. While absorption lines are rarely seen in the spectra of accretion discs, it is not unprecedented. For example, Strader et al. (2016) identified two sets of absorption lines in spectra of the neutron star X-ray binary 3FGL J0427.9−6704, which corresponded to the stellar component and the accretion disc. The second set of absorption lines track the reflex motion of the neutron star primary and also matched the velocities derived from the emission features associated with the accretion disc. Given that we are able to model the absorption lines with that of a stellar spectrum, it is unlikely that they emerge from an accretion flow.

The properties of the companion to 2M0412 are well explained by single star MIST stellar models. Fig. 15 shows the position of the companion in $\log(g)$ versus $T_{\rm eff}$ and $\log(L)$ versus $T_{\rm eff}$ compared to the MIST (Choi et al. 2016; Dotter 2016) stellar tracks at [Fe/H] = −0.5. Its position is consistent with that of a lower giant with $M_{\rm comp} \gtrsim 1.9\ \rm M_\odot$. However, we note that the companion appears to rotate slower ($v_{\rm rot} \sin(i) \simeq 18\ \rm km\ s^{-1}$) than expected for an object that has accreted significant mass. El-Badry et al. (2022b) presents a detailed comparison between the properties of the companion and stellar models, and interprets the slow rotation of the companion as a result of tidal interactions.

6 CONCLUSIONS

The evolved, stripped red giant 2M04123153+6738486 with $T_{\rm eff,\ giant} \simeq 4000\ \rm K$, $L_{\rm giant} \simeq 150\ \rm L_\odot$, $R_{\rm giant} \simeq 25\ \rm R_\odot$ is in a $P = 81.2$ d interacting binary with a lower giant companion ($T_{\rm eff,\ giant} \simeq 5000$ K, $L_{\rm giant} \simeq 60\ \rm L_\odot$, and $R_{\rm comp} \simeq 11\ \rm R_\odot$). The ASAS-SN, ATLAS, *TESS*, and ZTF light curves show that 2M0412 is a Roche lobe filling ellipsoidal variable (Section 3.3, Fig. 9). The high-resolution Keck/HIRES and LBT/PEPSI spectra indicate that the giant is rapidly rotating (Section 3.3). We also detect a secondary component in the spectra (Fig. 5) and the RV cross-correlation function (Fig. 4), which implies a mass ratio of $q \simeq 0.201 \pm 0.010$ (Fig. 5).

PHOEBE models of the ellipsoidal variability (Section 3.3) give an orbital inclination $i_{\rm orb} \simeq 49.4^\circ$, the radius of the giant $R_{\rm giant} \simeq 26\ \rm R_\odot$, the mass of the giant $M_{\rm giant} \simeq 0.38\ \rm M_\odot$, and a companion mass of $M_{\rm comp} = 1.9\ \rm M_\odot$ for $q \simeq 0.2$. The inferred mass of the red giant ($M_{\rm giant} \simeq 0.38\ \rm M_\odot$) is far lower than expected (based on its luminosity and single star evolutionary tracks), which implies that the giant has been heavily stripped by binary interaction.

We can find BPASS binary models very similar to the observed system with both stellar and compact object companions, and in all cases the giant has been partly stripped by mass transfer. MESA models of the cases with a stellar companion, which are needed to properly predict the luminosity and temperature of the companion, predict that a stellar companion would be significantly hotter ($\log T_{\rm eff} \gtrsim 4.0$) and more luminous ($\log(L/\rm L_\odot) \gtrsim 1.5$) than allowed by the observed SED. A more detailed exploration of parameter space can, however, find binaries that match our observations (El-Badry et al. 2022b).

We also find a broad, phase variable H α emission line (Section 3.4, Fig. 10) which is likely due to an accretion disc. The properties of the H α emission are consistent with RLOF from the giant. We derive a *Swift XRT* X-ray flux limit corresponding to $L_{\rm X} \lesssim 2.9 \times 10^{31}$ ergs $\rm s^{-1}$ (Section 3.5).

ACKNOWLEDGEMENTS

We thank the anonymous referee for their comments. We thank Dr. J. Strader for a careful reading of this manuscript. We thank Dr. J. J. Eldridge for useful discussions on the BPASS models. We thank Dr. M. Pinsonneault and L. Cao for useful discussions. We thank Las Cumbres Observatory and its staff for their continued support of ASAS-SN. ASAS-SN is funded in part by the Gordon and Betty Moore Foundation through grants GBMF5490 and GBMF10501 to the Ohio State University, and also funded in part by the Alfred P. Sloan Foundation grant G-2021-14192.

TJ, KZS, and CSK are supported by NSF grants AST-1814440 and AST-1908570. TJ acknowledges support from the Ohio State Presidential Fellowship. TAT is supported in part by NASA grant 80NSSC20K0531. TAT acknowledges previous support from Scialog Scholar grant 24216 from the Research Corporation, from which this effort germinated. JTH is supported by NASA award 80NSSC21K0136. DH acknowledges support from the Alfred P. Sloan Foundation, the National Aeronautics and Space Administration (80NSSC18K1585, 80NSSC19K0379), and the National Science Foundation (AST-1717000). CB acknowledges support from the National Science Foundation grant AST-1909022.

Parts of this research were supported by the Australian Research Council Centre of Excellence for All Sky Astrophysics in 3 Dimensions (ASTRO 3D), through project number CE170100013 and the Australian Research Council Centre of Excellence for Gravitational Wave Discovery (OzGrav), through project number CE170100004.

Funding for the Sloan Digital Sky Survey IV has been provided by the Alfred P. Sloan Foundation, the U.S. Department of Energy Office of Science, and the Participating Institutions. SDSS-IV acknowledges support and resources from the Center for High-Performance Computing at the University of Utah. The SDSS web site is www.sdss.org.

SDSS-IV is managed by the Astrophysical Research Consortium for the Participating Institutions of the SDSS Collaboration including the Brazilian Participation Group, the Carnegie Institution

for Science, Carnegie Mellon University, the Chilean Participation Group, the French Participation Group, Harvard-Smithsonian Center for Astrophysics, Instituto de Astrofísica de Canarias, The Johns Hopkins University, Kavli Institute for the Physics and Mathematics of the Universe (IPMU)/University of Tokyo, the Korean Participation Group, Lawrence Berkeley National Laboratory, Leibniz Institut für Astrophysik Potsdam (AIP), Max-Planck-Institut für Astronomie (MPIA Heidelberg), Max-Planck-Institut für Astrophysik (MPA Garching), Max-Planck-Institut für Extraterrestrische Physik (MPE), National Astronomical Observatories of China, New Mexico State University, New York University, University of Notre Dame, Observatário Nacional/MCTI, The Ohio State University, Pennsylvania State University, Shanghai Astronomical Observatory, United Kingdom Participation Group, Universidad Nacional Autónoma de México, University of Arizona, University of Colorado Boulder, University of Oxford, University of Portsmouth, University of Utah, University of Virginia, University of Washington, University of Wisconsin, Vanderbilt University, and Yale University.

This work has made use of data from the European Space Agency (ESA) mission *Gaia* (https://www.cosmos.esa.int/gaia), processed by the *Gaia* Data Processing and Analysis Consortium. This publication makes use of data products from the Two Micron All Sky Survey, as well as data products from the Wide-field Infrared Survey Explorer. This research was also made possible through the use of the AAVSO Photometric All-Sky Survey (APASS), funded by the Robert Martin Ayers Sciences Fund.

The LBT is an international collaboration among institutions in the United States, Italy, and Germany. LBT Corporation partners are: The University of Arizona on behalf of the Arizona Board of Regents; Istituto Nazionale di Astrofisica, Italy; LBT Beteiligungsgesellschaft, Germany, representing the Max-Planck Society, The Leibniz Institute for Astrophysics Potsdam, and Heidelberg University; The Ohio State University, representing OSU, University of Notre Dame, University of Minnesota, and University of Virginia.

PEPSI was made possible by funding through the State of Brandenburg (MWFK) and the German Federal Ministry of Education and Research (BMBF) through their Verbundforschung grants 05AL2BA1/3 and 05A08BAC.

This research is based on observations made with the *Neil Gehrels Swift Observatory*, obtained from the MAST data archive at the Space Telescope Science Institute, which is operated by the Association of Universities for Research in Astronomy, Inc., under NASA contract NAS 5-26555. This paper includes data collected with the *TESS* mission, obtained from the MAST data archive at the Space Telescope Science Institute (STScI). Funding for the *TESS* mission is provided by the NASA Explorer Program. STScI is operated by the Association of Universities for Research in Astronomy, Inc., under NASA contract NAS 5-26555.

Some of the data presented herein were obtained at the W. M. Keck Observatory, which is operated as a scientific partnership among the California Institute of Technology, the University of California, and the National Aeronautics and Space Administration. The Observatory was made possible by the generous financial support of the W. M. Keck Foundation.

This research is based on observations obtained with the *Samuel Oschin Telescope* 48-inch and the 60-inch Telescope at the Palomar Observatory as part of the Zwicky Transient Facility project. ZTF is supported by the National Science Foundation under Grant No. AST-2034437 and a collaboration including Caltech, IPAC, the Weizmann Institute for Science, the Oskar Klein Center at Stockholm University, the University of Maryland, Deutsches Elektronen-Synchrotron and Humboldt University, the TANGO Consortium of Taiwan, the University of Wisconsin at Milwaukee, Trinity College Dublin, Lawrence Livermore National Laboratories, and IN2P3, France. Operations are conducted by COO, IPAC, and UW.

The authors wish to recognize and acknowledge the very significant cultural role and reverence that the summit of Maunakea has always had within the indigenous Hawaiian community. We are most fortunate to have the opportunity to conduct observations from this mountain.

We thank the ZTF and ATLAS projects for making their light-curve data publicly available. This research has made use of the VizieR catalogue access tool, CDS, Strasbourg, France. This research also made use of Astropy, a community-developed core Python package for Astronomy (Astropy Collaboration et al. 2013, 2018).

DATA AVAILABILITY

The photometric data are all publicly available. The spectra will be shared on reasonable request to the corresponding author.

REFERENCES

Abdul-Masih M. et al., 2020, Nature, 580, E11
Adams S. M., Kochanek C. S., 2015, MNRAS, 452, 2195
Arentsen A., Starkenburg E., Shetrone M. D., Venn K. A., Depagne É., McConnachie A. W., 2019, A&A, 621, A108
Astropy Collaboration et al., 2013, A&A, 558, A33
Astropy Collaboration et al., 2018, AJ, 156, 123
Bailer-Jones C. A. L., Rybizki J., Fouesneau M., Demleitner M., Andrae R., 2021, AJ, 161, 147
Bayo A., Rodrigo C., Barrado Y Navascués D., Solano E., Gutiérrez R., Morales-Calderón M., Allard F., 2008, A&A, 492, 277
Beech M., 1985, Ap&SS, 117, 69
Bellm E. C. et al., 2019, PASP, 131, 018002
Bianchi L., Conti A., Shiao B., 2014, Adv. Space Res., 53, 900
Blanco-Cuaresma S., 2019, MNRAS, 486, 2075
Blanco-Cuaresma S., Soubiran C., Heiter U., Jofré P., 2014, A&A, 569, A111
Blanton M. R. et al., 2017, AJ, 154, 28
Bodensteiner J. et al., 2020, A&A, 641, A43
Boothroyd A. I., Sackmann I. J., 1988, ApJ, 328, 641
Bovy J., Rix H.-W., Green G. M., Schlafly E. F., Finkbeiner D. P., 2016, ApJ, 818, 130
Breeveld A. A. et al., 2010, MNRAS, 406, 1687
Burrows D. N. et al., 2005, Space Sci. Rev., 120, 165
Cardelli J. A., Clayton G. C., Mathis J. S., 1989, ApJ, 345, 245
Castelli F., Kurucz R. L., 2003, in Piskunov N., Weiss W. W., Gray D. F., eds, Proc. IAU Symp. 210, Modelling of Stellar Atmospheres. Astron. Soc. Pac., San Francisco, p. A20
Chambers K. C. et al., 2016, preprint (arXiv:1612.05560)
Chawla C., Chatterjee S., Breivik K., Krishna Moorthy C., Andrews J. J., Sanderson R. E., 2021, preprint (arXiv:2110.05979)
Chen X., Wang S., Deng L., de Grijs R., Yang M., Tian H., 2020, ApJS, 249, 18
Choi J., Dotter A., Conroy C., Cantiello M., Paxton B., Johnson B. D., 2016, ApJ, 823, 102
Claret A., 2017, A&A, 600, A30
Claret A., Bloemen S., 2011, A&A, 529, A75
Collier A. C., Jenkins C. R., 1984, MNRAS, 211, 391
Conroy K. E. et al., 2020, ApJS, 250, 34
Demircan O., 1987, Ap&SS, 137, 195
Dinçer T., Bailyn C. D., Miller-Jones J. C. A., Buxton M., MacDonald R. K. D., 2018, ApJ, 852, 4
Dixon D., Tayar J., Stassun K. G., 2020, AJ, 160, 12
Dotter A., 2016, ApJS, 222, 8
Drimmel R., Cabrera-Lavers A., López-Corredoira M., 2003, A&A, 409, 205
Eggleton P. P., 1983, ApJ, 268, 368
El-Badry K., Burdge K., 2022, MNRAS, 511, L24

El-Badry K., Quataert E., 2020, MNRAS, 493, L22
El-Badry K., Quataert E., 2021, MNRAS, 502, 3436
El-Badry K., Rix H.-W., Quataert E., Kupfer T., Shen K. J., 2021, MNRAS, 508, 4106
El-Badry K., Burdge K. B., Mróz P., 2022a, MNRAS, 511, 3089
El-Badry K., Seeburger R., Jayasinghe T., Rix H.-W., Almada S., Conroy C., Price-Whelan A. M., Burdge K., 2022b, MNRAS, 512, 5620
Eldridge J. J., Stanway E. R., 2016, MNRAS, 462, 3302
Eldridge J. J., Stanway E. R., Xiao L., McClelland L. A. S., Taylor G., Ng M., Greis S. M. L., Bray J. C., 2017, Publ. Astron. Soc. Aust., 34, e058
Elitzur M., Ivezić Ž., 2001, MNRAS, 327, 403
Fender R. P., Russell D. M., Knigge C., Soria R., Hynes R. I., Goad M., 2009, MNRAS, 393, 1608
Foreman-Mackey D., Hogg D. W., Lang D., Goodman J., 2013, PASP, 125, 306
Gagné J. et al., 2018, ApJ, 856, 23
Gaia Collaboration, 2021, A&A, 649, A1
Giesers B. et al., 2018, MNRAS, 475, L15
Giesers B. et al., 2019, A&A, 632, A3
Green G. M., Schlafly E., Zucker C., Speagle J. S., Finkbeiner D., 2019, ApJ, 887, 93
Gunn J. E. et al., 2006, AJ, 131, 2332
Gustafsson B., Edvardsson B., Eriksson K., Jørgensen U. G., Nordlund Å., Plez B., 2008, A&A, 486, 951
Heinze A. N. et al., 2018, AJ, 156, 241
Henden A. A., Levine S., Terrell D., Welch D. L., Munari U., Kloppenborg B. K., 2018, American Astronomical Society Meeting Abstracts, #223.06
HI4PI Collaboration et al., 2016, A&A, 594, A116
Hogg D. W., Eilers A.-C., Rix H.-W., 2019, AJ, 158, 147
Horvat M., Conroy K. E., Pablo H., Hambleton K. M., Kochoska A., Giammarco J., Prša A., 2018, ApJS, 237, 26
Howard A. W. et al., 2010, ApJ, 721, 1467
Irrgang A., Geier S., Kreuzer S., Pelisoli I., Heber U., 2020, A&A, 633, L5
Ivezic Z., Elitzur M., 1997, MNRAS, 287, 799
Janssens S. et al., 2022, A&A, 658, A129
Jayasinghe T. et al., 2018, MNRAS, 477, 3145
Jayasinghe T. et al., 2021a, MNRAS, 503, 200
Jayasinghe T. et al., 2021b, MNRAS, 504, 2577
Jorissen A., Boffin H. M. J., Karinkuzhi D., Van Eck S., Escorza A., Shetye S., Van Winckel H., 2019, A&A, 626, A127
Kochanek C. S. et al., 2017, PASP, 129, 104502
Kolb U., Ritter H., 1990, A&A, 236, 385
Kolbl R., Marcy G. W., Isaacson H., Howard A. W., 2015, AJ, 149, 18
Langer N. et al., 2020, A&A, 638, A39
Lennon D. J., Dufton P. L., Villaseñor J. I., Evans C. J., Langer N., Saxton R., Monageng I. M., Toonen S., 2021, preprint (arXiv:2111.12173)
Lenz P., Breger M., 2005, Commun. Asteroseismology, 146, 53
Lindegren L. et al., 2021a, A&A, 649, A2
Liu J. et al., 2019, Nature, 575, 618
Marshall D. J., Robin A. C., Reylé C., Schultheis M., Picaud S., 2006, A&A, 453, 635
Martin D. V. et al., 2019, A&A, 624, A68
Masci F. J. et al., 2019, PASP, 131, 018003
Mazzola Daher C. et al., 2022, MNRAS, 512, 2051
Miller A., Kounkel M., Sun M., Dixon D., Boggio C., Covey K. R., Stassun K. G., Mathieu R., 2021, AJ, 162, 131
Morrissey P. et al., 2007, ApJS, 173, 682
Mortier A. et al., 2016, A&A, 585, A135
Orosz J. A., Bailyn C. D., Remillard R. A., McClintock J. E., Foltz C. B., 1994, ApJ, 436, 848
Paczynski B., 1977, ApJ, 216, 822
Paxton B., Bildsten L., Dotter A., Herwig F., Lesaffre P., Timmes F., 2011, ApJS, 192, 3
Paxton B. et al., 2013, ApJS, 208, 4
Paxton B. et al., 2015, ApJS, 220, 15
Paxton B. et al., 2018, ApJS, 234, 34
Paxton B. et al., 2019, ApJS, 243, 10
Peters G. J., 2001, in Vanbeveren D., ed., Astrophysics and Space Science Library, Vol. 264, The Influence of Binaries on Stellar Population Studies. Kluwer, Dordrecht, p. 79
Petigura E. A., 2015, PhD thesis, Univ. Calif., Berkeley
Poole T. S. et al., 2008, MNRAS, 383, 627
Price-Whelan A. M., Goodman J., 2018, ApJ, 867, 5
Price-Whelan A. M., Hogg D. W., Foreman-Mackey D., Rix H.-W., 2017, ApJ, 837, 20
Prša A. et al., 2016, ApJS, 227, 29
Ramírez I., Allende Prieto C., Lambert D. L., 2013, ApJ, 764, 78
Ricker G. R. et al., 2015, J. Astron. Telesc. Instrum. Syst., 1, 014003
Rivinius T., Baade D., Hadrava P., Heida M., Klement R., 2020, A&A, 637, L3
Roming P. W. A. et al., 2005, Space Sci. Rev., 120, 95
Rowan D. M., Stanek K. Z., Jayasinghe T., Kochanek C. S., Thompson T. A., Shappee B. J., Holoien T. W. S., Prieto J. L., 2021, MNRAS, 507, 104
Saracino S. et al., 2022, MNRAS, 511, 2914
Schönrich R., Binney J., Dehnen W., 2010, MNRAS, 403, 1829
Ségransan D. et al., 2011, A&A, 535, A54
Shao Y., Li X.-D., 2019, ApJ, 885, 151
Shappee B. J. et al., 2014, ApJ, 788, 48
Shenar T. et al., 2020, A&A, 639, L6
Skrutskie M. F. et al., 2006, AJ, 131, 1163
Smak J., 1981, Acta Astron., 31, 395
Stanway E. R., Eldridge J. J., 2018, MNRAS, 479, 75
Stevance H., Eldridge J., Stanway E., 2020, J. Open Source Softw., 5, 1987
Stevance H. F., Parsons S. G., Eldridge J. J., 2022, MNRAS, 511, L77
Strader J. et al., 2015, ApJ, 804, L12
Strader J., Li K.-L., Chomiuk L., Heinke C. O., Udalski A., Peacock M., Shishkovsky L., Tremou E., 2016, ApJ, 831, 89
Strassmeier K. G. et al., 2015, Astron. Nachr., 336, 324
Strassmeier K. G., Ilyin I., Steffen M., 2018, A&A, 612, A44
Tayar J. et al., 2015, ApJ, 807, 82
Thompson T. A. et al., 2019, Science, 366, 637
Tonry J. L. et al., 2018, PASP, 130, 064505
Torres M. A. P., Casares J., Martínez-Pais I. G., Charles P. A., 2002, MNRAS, 334, 233
Trimble V. L., Thorne K. S., 1969, ApJ, 156, 1013
Vallely P. J., Kochanek C. S., Stanek K. Z., Fausnaugh M., Shappee B. J., 2021, MNRAS, 500, 5639
Verbunt F., Phinney E. S., 1995, A&A, 296, 709
Vogt S. S. et al., 1994, in Crawford D. L., Craine E. R., eds, Proc. SPIE Conf. Ser. Vol. 2198, Instrumentation in Astronomy VIII. SPIE, Bellingham, p. 362
Wade R. A., Horne K., 1988, ApJ, 324, 411
Wilson J. C. et al., 2019, PASP, 131, 055001
Wright E. L. et al., 2010, AJ, 140, 1868
Zheng L.-L. et al., 2019, AJ, 158, 179

This paper has been typeset from a TEX/LATEX file prepared by the author.